Measurement 266 (2026) 120339

Contents lists available at ScienceDirect

Measurement

journal homepage: www.elsevier.com/locate/measurement

Phase-space-based fusion of angular and height data in tactile and optical surface texture measurement for tribological analysis

Matthias Eifler [a,*], Boris Brodmann [b]

[a] IU International University of Applied Sciences, Juri-Gagarin Ring 152, 99084 Erfurt, Germany
[b] OptoSurf GmbH, Nobelstraße 9-13, 76275 Ettlingen, Germany

ABSTRACT

Accurate characterization of surface topography is essential for understanding and optimizing tribological processes. A wide range of tactile and optical measurement techniques – such as stylus profilometry, scattered light sensors, white light interferometry, confocal microscopy, and focus variation – are available, each with distinct advantages and inherent nonlinearities that may introduce method-specific artefacts. This study introduces a novel approach for mapping and assessing surface topography using a phase-space representation that integrates both height and angular information and enables a joint analysis and fusion of both characteristics. This exhibits potential for efficient and compact monitoring of tribological processes. We investigate the informational content and limitations of various measurement techniques by surface texture and angular parameters, highlighting the differences and the impact of the statistics of a surface. Then, the overall height and angular distributions of the measured topographies are compared. Angular representations offer an additional dimension of analysis, enhancing the robustness of surface characterization. For the angular distribution, tactile and optical methods often yield differing results, particularly for complex surface features. A direct angular measurement offers another perspective on the surface topography and the combination of height and angular information enables a more holistic surface description. The proposed phase-space representation is exemplified through the analysis of cylinder liner surfaces, illustrating its potential to improve the accuracy and interpretability of tribological assessments and demonstrating the potential of this representation to expose even slightest changes in the surface topography. The fusion of the independent variables height and slope can allow a precise monitoring of tribological processes where only one of the two distributions may change and thus allows a novel perspective on the tribological assessment of surfaces.

1. Introduction

When tribological processes like friction, wear, and lubrication are examined, they are directly related to the microgeometry of the surface – which is the boundary responsible for the interaction of a workpiece with other objects or its environment [1]. A significant paradigm shift has emerged: surfaces are now recognized as having functional requirements that are intrinsically linked to their defined microstructures [2].

Surface texture is assessed using specialized measuring instruments, each designed to capture the actual surface characteristics with minimal deviation. Despite the precision of modern surface texture measuring instruments, each instrument introduces specific influences that affect both the accuracy of the results and the nature of the information obtained. These instrument-specific characteristics – ranging from resolution limits to sensitivity with regard to certain surface features – can lead to discrepancies in the interpretation of surface topography when comparing different measuring instruments and/or principles. In this paper, we investigate how such variations impact the characterization of tribologically relevant surfaces. Furthermore, we explore the potential benefits of integrating multiple measurement representations, demonstrating how using the analytical framework of a combined phase-space approach can enhance the reliability and depth of surface analysis and can lead to a more comprehensive tribological characterization of surfaces. The integration of height and angular data as statistically independent variables and the resulting analytical framework can link the morphology of a surface to its tribological behavior.

2. State of the art

2.1. Surface topography measurement

To assess whether a surface fulfills its intended functional characteristics, surface texture is commonly measured by capturing the distance between the sensor and the workpiece. This measurement forms the basis for reconstructing either a profile section or a full areal topography, depending on the technique used. Such data is essential for linking surface structure to performance, particularly in tribological applications. The corresponding fundamental developments of the first research projects in the surface topography assessment using areal

---

* Corresponding author.
E-mail address: matthias.eifler@iu.org (M. Eifler).

https://doi.org/10.1016/j.measurement.2026.120339
Received 5 September 2025; Received in revised form 1 December 2025; Accepted 5 January 2026

techniques were described in the “Blue book” [1], and “Green book” [3]. Additionally, Leach et al. [4] have also summarized case studies regarding tribological systems including cylinder liners.

To establish a foundation for comparing different surface measurement techniques, it is essential to examine the underlying physical principles of tactile and optical methods: Tactile surface measurement is based on the principles of contact mechanics. In this approach, a stylus physically traverses the surface, and the recorded signal corresponds to the trajectory of the center of the stylus tip – the mechanical profile can thus be described as the path of a spherical body rolling over the surface [5]. The resulting mechanical surface profile is inherently influenced by mechanical material properties such as Young’s modulus and Poisson’s ratio. The stylus-based measuring instrument, which remains the most widely used method for industrial surface texture characterization, captures profile measurements and has been in practical application for approximately a century [3]. Its resolution capabilities and fidelity of tactile measurements are determined by the morphological filtering by the stylus tip geometry in the lateral direction, and Hertzian contact stresses in the vertical direction [6].

Since the 1980s, optical surface topography measurement techniques have gained increasing attention due to their ability to rapidly acquire areal surface texture data in a single measurement [4]. Commonly employed optical methods include interferometric techniques such as white-light interferometry, as well as confocal microscopy and focus variation [4]. Optical surface texture measurement is governed by electromagnetic theory, particularly Maxwell’s equations. These methods rely on the interaction of light with the surface, capturing what can be described as the electromagnetic surface. The measurement outcome is shaped by the optical properties of the material, such as dielectric constant, refractive index, and electrical conductivity [7]. Optical resolution in surface texture measurement is fundamentally limited by diffraction effects and the depth of field of the optical system [7]. The considerations show that each technique is subject to distinct physical constraints and interpretive models, which must be carefully considered when comparing data across systems – especially in tribological applications where surface function is closely tied to microstructures.

Moreover, the data formats that are produced by these methods most often differ significantly. Industrial tactile instruments typically generate profile (“2D”) data, as they acquire a single trace across the surface. Optical surface texture measuring instruments, on the other hand, commonly produce areal data (“2.5D”), offering a more comprehensive and statistically reliable spatial representation of the surface topography [4].

2.2. Surface topography evaluation

To ensure that the requirements, e.g. a defined behaviour in the tribological scenarios of wear, lubrication or friction, are fulfilled by the workpiece, a measurement of the surface topography is often required. Quantitative methods for characterizing surface topography have been in use since the early 20th century [3]. As surface texture parameters began to emerge, it became evident by the 1940 s that relying solely on parameters like R_a and R_t – which as mean value and span describe characteristics of the overall height distribution – was insufficient, prompting the search for more comprehensive alternatives [1]. Since the amplitude-based parameters are easy and convenient to understand, even though R_a is “extremely limited in value” [3] it is still the most common profile surface texture parameter, even in the context of scientific functional characterization [8]. In the ensuing decades to the 1940s, numerous new parameters for evaluating surface texture were introduced. However, in 1982, Whitehouse critically addressed this proliferation in his influential publication titled “The parameter rash – is there a cure?” [9]. Nonetheless, the 1980s also marked significant progress in functional surface characterization. The development of the R_k parameters – based on the Abbott-Firestone curve – enabled more targeted assessments of wear, lubrication, and friction, culminating in the establishment of DIN 4776 in 1990 [10]. This category of function-oriented parameters is often used for evaluating surfaces such as plateau-honed textures, enabling the analysis of surface characteristics related to the material ratio as a function of topography height – such as oil retention volume – on both round- and sharp-ridged surfaces [10]. The associated international standard, ISO 13565-2 [11], was subsequently introduced. More recently, its parameters R_k, R_{pk}, R_{vk}, Mr_1, and Mr_2 – designed to address certain limitations of previously applied amplitude-based parameters – have also been incorporated into the new standard for profile texture analysis ISO 21920-2 [12]. In parallel, an approach to characterize functional surface properties based on height distribution using the material probability curve was developed with the parameters R_{pq}, R_{mq}, and R_{vq} – later standardized in ISO 13565-3 [13]. This group of parameters has also been incorporated into the latest profile standardization of ISO 21920-2 [12].

With the advent of areal surface texture standardization, analogous areal parameters: S_k, S_{pk}, S_{vk}, S_{mr1}, S_{mr2}, S_{pq}, S_{mq}, and S_{vq} were defined in ISO 25178-2 [14]. The R_k and S_k parameters have gained broad industrial acceptance, particularly in Europe [15], which was also confirmed by an industrial survey [16], while the R_q and S_q parameters - R_{pq}, R_{mq}, and R_{vq} and their areal equivalents - that were developed in the United States, are more commonly applied there which was stated by Pawlus both in the context of cylinder liners [17] and in the general context of functional characterization [18].

The design and application of surfaces featuring defined functional characteristics is an ongoing paradigm shift [2] and various applications have been described in the literature: Pawlus et al. [18] reviewed the historical development of functional surface texture parameters and demonstrated their application through a series of four successive honing processes used in the production of cylinder liners. The evaluation of results was based on a truncation model [18]. It was demonstrated that the ISO 13565-3 parameters feature a correlation to manufacturing parameters, e.g. the grit size and plateau honing time [17]. Volume-based analysis was shown to correlate with hill and dale properties [19] and just as well as feature-based analysis can serve as an alternative to functional surface texture parameters [20]. Also, parameters that assess the directionality have been correlated with functional characteristics like wear [21] or plastic deformation [22]. Functional surface texture parameters can be used for performance verification of surface texture measuring instruments for both profile [23] and areal applications [24].

Over the decades, more than 100 different profile surface texture parameters have been described [3] which was criticized by Whitehouse [9], but also alternative approaches for functional characterization have been described: Neural networks were used for process classification and surface texture parameter prediction [25] and the prediction of the Abbott-Firestone-Curve using gray-scale images was examined [26]. Additionally, direct virtual testing regarding functional characteristics has been proposed [27], as well as analyses using the discrete Fourier transform [28], the auto-correlation function for the simulation of ground or honed surfaces [29], and generically non-Gaussian surfaces [30]. Applications of the equivalent in the frequency domain, the Power Spectral Density (PSD), have also been examined for surface generation [31], as well as for the assessment of quality [32], and the prediction of tribological characteristics [33].

2.3. Comparisons of tactile and optical methods

It has been described that tactile and optical measurements show limited comparability due to the different physical effects inherent in their operating principles. When considering practical aspects, also different perspectives can be established: when the common models of signal processing are applied, surface texture measuring instruments can generally be considered as low-pass filters, that feature a certain cut-off frequency in their transmission behavior. Using e.g. a digital filter based on the auto-regressive moving average (ARMA) model, the transfer behavior of stylus instruments, confocal microscopes, white-light interferometers or chromatic confocal sensors can be approximated [34]. Empirical comparisons using material measures with well-defined rectangular and sinusoidal surface structures demonstrated that this linear model yields good agreement across various instrument types [34]. The model can also be extended for certain measurement principles when non-linear effects are considered, as e.g. described for confocal microscopes, where the model enables virtual measurement [35].

The fact that these non-linear transfer effects are specific to the measurement principle can again be reasoned with the physical differences – mostly the structures featuring large inclinations or curvatures are challenging to measure for many optical surface texture measuring instruments [36]. Since these structures often occur notably in functionally relevant surfaces, differences in the transmission of e.g. valleys can be observed when the distributions of their heights, widths and areas are compared, as shown for the example of cylinder liners in [37]. In this study based on a set of six cylinder liners that were measured at the same location using a stylus instrument and confocal microscope, it could also be shown that some functional surface texture parameters can differ significantly between these methods [37].

For profile material measures as measuring objects, there have also been several comparisons of the assessment of surface texture parameters using tactile and optical surface topography measuring instruments: A comparison of a sinusoidal geometry and a lapped surface showed significant differences in 2002 [38]. At that time, one key reason for the differences was identified with the missing calibration and standardization frameworks for optical surface topography measuring instruments [38]. Koenders et al. in contrast conducted step height measurements using different measuring principles and concluded that a “good agreement” of most results was achieved [39]. For other comparisons of the profile material measures of ISO 5436-1 the results often highlighted differences in the transfer behavior between different measuring instruments even when applying the identical measurement principle: Doytchinov et al. applied several stylus instruments for step height measurement, sinusoidal surfaces and profile roughness material measures and could observe a good agreement [40], whereas a comparison between different atomic force microscopes (AFM) based on step heights illustrated that parts of the instruments exhibited notable uncertainties [41]. The last results were confirmed by another comparison stating that even results generated by highly precise surface texture measuring instruments should be “very carefully examined” in the context of calibration [42]. Other comparisons based on profile material measures showed either a “mixed” performance [43], “a relatively large number of inconsistent results” [44] or in some cases also a relatively good agreement even when different measuring principles were considered [45] which illustrates the complexity and large number of influencing factors on surface texture measurement.

Most surface texture parameters have the limitation that they are only based on the statistical height distribution, even though not only the occurrence of non-linear effects but also the functional characteristics of surface structures are often not shaped by height values, but for example the slope or curvature of the surface: Coulomb was among the first to recognize that friction between contacting surfaces arises from the mechanical interlocking of surface asperities [46]. This observation underscores the critical role of surface topography in determining the real contact area and, consequently, the frictional behavior. This concept was further developed in the Greenwood-Williamson model, which demonstrated that, in addition to material properties such as hardness and Young’s modulus, the microtopography of the contacting surfaces significantly influences the elastic and plastic deformation within the contact area [47]. According to Greenwood and Williamson, the transition between elastic and plastic deformation in surface contact is primarily governed by the statistical properties of the surface topography, particularly the mean squared height deviations and the radii of the contacting asperities [47]. Their model has been extensively studied and applied across various domains, with significant attention given to both its theoretical foundations and the determination of its input parameters, e.g. for the modelling of cylinder liners [48,49]. Numerous approaches have been proposed and investigated for the determination of the plasticity index, with a comprehensive overview provided by Whitehouse ([50], p. 668 ff.). As an alternative to direct topographical analysis, frequency-dependent methods have also been suggested for estimating the contact area. One such approach involves the use of the autocorrelation function, which captures spatial frequency characteristics of the surface and offers insight into the distribution and interaction of asperities [51]. Based on the different physics, the results of height topography measurement depend on the measuring principle. However, also the evaluation of other characteristics than the height distribution, such as the angular distribution, can be useful for the characterization of the functional behavior of a surface.

2.4. Direct angular measurement

Another surface parameter that has been shown to correlate strongly with the real contact area is the surface gradient. Numerical simulations have demonstrated a clear relationship between the gradient and the extent of actual contact [52]. Popov further emphasized the relevance of this parameter by identifying the surface gradient as one of the principal descriptors in a generalized friction law for surfaces, highlighting its importance in characterizing tribological behavior [53]. The determination of the surface gradient, obtained as the derivative of a measured surface topography, presents significant challenges due to the high sensitivity of numerical differentiation to the measurement uncertainty. Even minor deviations in the measured height topography can lead to substantial errors in the computed gradient, particularly in the case of short-wavelength features, which are often represented by only a few data points. This issue has been discussed by Whitehouse in the context of hybrid surface texture parameters ([50], p. 15), highlighting the limitations of gradient-based analyses in the presence of measurement noise. As however the gradient and its associated parameters like R_{dq} correlate with tribological characteristics like the friction on general lapped or ground surfaces [54], or the friction coefficient of worm flanks [55], other methods for a direct measurement have been developed e.g. with angular-resolved scattering light measurement. This measurement technique features potential for a functional characterization of surface topography using the angular distribution and is well-suited for an inline application [56]. It can be implemented using a traceability chain [57] and the statistical parameters of the scattering light distribution can be correlated with parameters of machining processes, illustrating its potential for process monitoring, see. e.g. [58]. Since the height distribution and angular distribution of a surface topography are independent statistical variables – e.g. by changing the order of the surface height values the angular distribution can be altered without changing the statistics of the heights – the distribution of heights and angles features complementary information that can be used for the monitoring of tribological processes. This independence was confirmed in a previous study [59]. In the following, a study is presented to describe a combined view on the surface using both the angular and height perspectives, suggesting a more comprehensive approach for the monitoring of both tribological processes and the state of a manufacturing processes.

3. Methodology

3.1. Samples

It has been shown that there are at last three different perspectives on the surface: profile data using stylus instruments, areal data using optical instruments, and angular data using scattering light measurement. To examine the information content in the different representations and to compare to what degree the combination of these different perspectives can provide a comprehensive view on the surface topography and the associated functional characteristics of the surface, a case study was conducted. For this case study a typical use-case with high functional requirements was selected. 15 different cylinder liner surfaces that are representative for a workpiece with a high functional relevance and high functional requirements were chosen so that different roughness characteristics and amplitudes are represented. The samples used in this study were selected from a larger collection of cylinder liners and exhibit a broad range of surface characteristics. These include pronounced plateau structures – either fine or coarse – as well as distinct grooves, embedded particles, and varying degrees of stochastic or deterministic surface features. Some examples are summarized in Fig. 1 which shows examples for a plateau-based surface (CL 1), a stochastic surface (CL 3) and a surface featuring embedded particles (CL 4). The groove depths also differ significantly among the samples. Each specimen was characterized using multiple measurement techniques, which are described in detail in the following.

3.2. Topography measurements

A multi-measurement approach provides enriched information on surface morphology, thereby reinforcing the robustness of metrological results. The feasibility and effectiveness of this general approach have been validated. To establish a perspective onto the surface based on the topography heights and angles, measurements were taken using three different methods – the geometric relations are summarized in Fig. 2 and the profile-based measurements were determined in direction of the cylinder's axis of rotation. It was not desired to perform the measurements at the exact same positions but rather cover an area of each sample as large as possible to receive a dataset that is representative for the overall state of the surface and can describe its statistics. The following methods were used:

(a) Profile measurement: Surface profile texture measurements were conducted using the stylus-based instrument Hommel-Etamic Nanoscan 855. For each specimen, a total of 25 individual profiles were recorded, spaced laterally at intervals of 0.5 mm to ensure statistical representativeness of the surface characteristics. Each profile extended over a minimum sampling length of 80 mm. Accounting for the filter's running-in and running-out lengths, five discrete evaluation segments of 12.5 mm each were extracted from every profile, based on a standardized segment length of 15 mm.

The data acquisition parameters were defined as follows: the sampling interval was set to $\Delta x = 0.5\,\mu\mathrm{m}$, and the scanning velocity was maintained at $0.5mm/s$ to minimize dynamic effects and ensure a stable interaction between stylus probe and workpiece. This results in an overall measurement time of approximately 1.1 h per cylinder liner. The stylus employed for measurement featured a tip radius of $r_{tip} = 5\mu m$, ensuring adequate resolution for capturing fine surface features. The 125 evaluation positions with a length of 12.5 mm each consist of 3.125 Mio. measured height values per cylinder liner.

(b) Areal measurement: Areal surface topographies were determined using the confocal microscope NanoFocus μSurf, equipped with a 20× objective lens, yielding a field of view of 800 μm × 800 μm. To obtain a sufficiently large evaluation area, multiple adjacent measurements were stitched together, resulting in a composite surface map of approximately 0.7 mm × 18 mm highlighted in Fig. 2b which takes about 20–30 min to measure per cylinder liner.

The lateral spacing in both lateral directions is defined as $\Delta x = \Delta y = 1.57\mu m$, enabling the extraction of 400 individual profile datasets with a lateral spacing of Δy from the areal dataset. For profile-based analysis, segments of 15 mm length were extracted from the central region of each profile, allowing for an evaluation length of 12.5 mm after accounting for filter running-in and running-out lengths. Consequently, the central 15 mm of each of the 400 profiles within the stitched areal dataset was utilized for detailed surface texture evaluation. The 400 evaluation positions with a length of 12.5 mm each consist of approximately 3.185 Mio. height values per cylinder liner and therefore a similar number as the tactile measurements.

c) Optical angular measurement: Surface measurements were conducted using an angular-resolved scattering light (ARS) sensor of the type OptoSurf OS 500. A lens capable of projecting surface angle intensities within a ±16° range onto the sensor array was employed. The measurement setup is illustrated in Fig. 3. 50 profiles were scanned with a length of 20 mm each. The profiles featured a lateral distance of 20 μm between each other. 1,250 measurements per profile were conducted with a spacing of $\Delta x = 16\mu m$, leading to an overall number of 62,500 evaluations per cylinder liner within a measurement time of $<$2 min per cylinder liner. The procedure was repeated for the two different light-spot diameters 900 μm and 30 μm.

3.3. Topography evaluation

(a) Stylus instrument profile data: A total least squares straight line fit was applied to the full $>$80 mm profile as a pre-processing step prior to interpolation to an equidistant spacing of $\Delta x = 0.5\mu m$. Subsequently, the center of each of the 25 profiles was identified, and five evaluation segments of $15mm$ each were symmetrically extracted around this center, ensuring no overlap. This resulted in a total evaluation length of $5 \cdot 15\ \mathrm{mm} = 75\ \mathrm{mm}$ per profile used for data analysis and 125 evaluation positions in total. For each 15 mm segment, the following pre-processing steps were applied in accordance with ISO 21920-2 and since almost all cylinder liners feature a relatively large roughness amplitude, the parameters of setting class (SC) 4 defined in ISO 21920-3 were selected as follows:

(i) S-filtering was performed using a linear Gaussian filter in accordance with ISO 16610-21, applying a nesting index of $N_{is} = 8\mu\mathrm{m}$.

(ii) The F-operation was carried out by removing a fitted least squares straight line from each profile. The straight line represents the nominal geometry since profiles in the direction of each cylinder's axis of rotation were evaluated.

(iii) Given the generally stratified nature of the examined surfaces, L-filtering was performed using a robust Gaussian filter of second order, in accordance with ISO 16610-31. A nesting index of $N_{ic} = 2.5\mathrm{mm}$ was applied following the parameters for SC4 defined in ISO 21920-3.

(iv) Each profile segment was cropped to an evaluation length of $l_e = 12.5\mathrm{mm}$.

(v) The following surface texture parameters were evaluated for all profile segments as defined by ISO 21920-2: Amplitude parameters: R_a (arithmetic mean height), R_q (root mean square height), R_sk (skewness), R_ku (kurtosis), R_t (total height), hybrid parameters: R_dq (root mean square gradient), R_da (arithmetic mean of the absolute gradient), R_dt (maximum absolute gradient), R_dl (developed length), parameters for stratified surfaces using the material ratio curve: R_k (core height), R_pk (reduced peak height), R_vk (reduced pit depth), attribute parameters based on peak heights and pit depths: R_pmax (maximum peak height), R_p (mean peak height), R_vmax (maximum pit depth), R_v (mean pit depth), R_z (maximum height), parameters based on profile elements: R_sm (mean profile element spacing), R_c (mean profile element height), R_cmax (maximum profile element height), $R_\mathrm{sm}\,count$ (no. of profile elements). The parameters were determined using the algorithms described in [60] and represent the most common groups of surface texture parameters that are available in the international standardization.

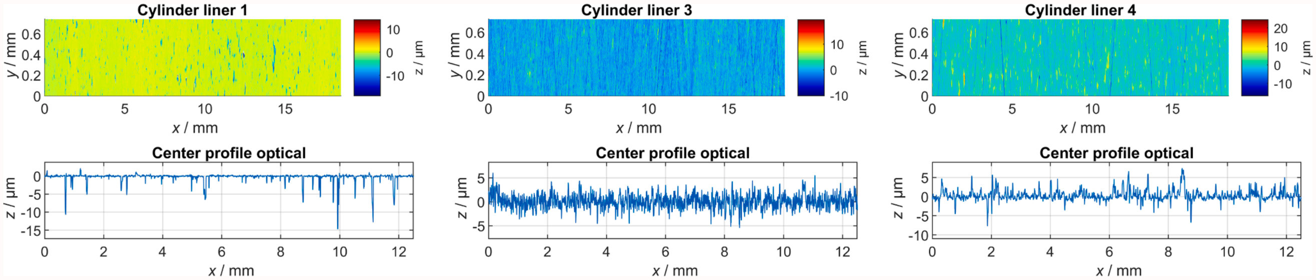

Fig. 1. Examples for different surface types present in the set of cylinder liners: stratified surface (CL 1), stochastic surface (CL 3), and surface featuring particles (CL 4).

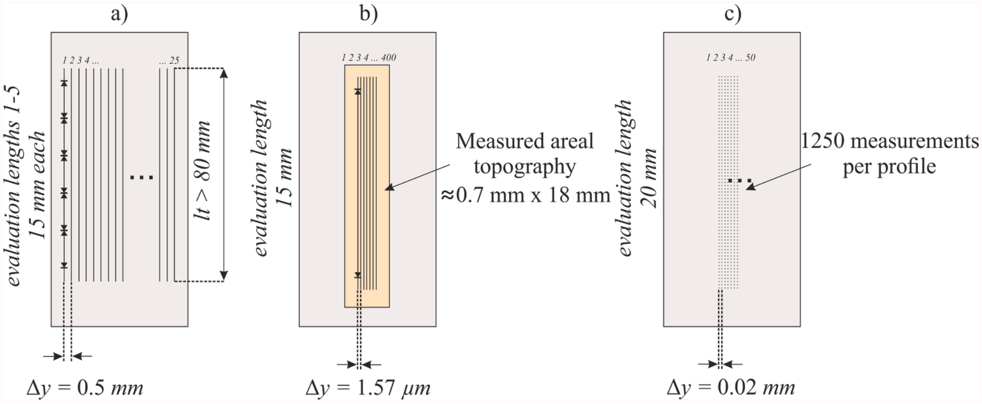

Fig. 2. Overview of measurement positions for the three applied methods [59]: (a) Tactile texture measurement: 25 profiles, each at least 80 mm in length. Every profile was subdivided into five evaluation segments of 15 mm each. (b) Optical texture measurement: A stitched surface topography of approximately 18 mm in length was acquired. From this, 400 central profiles were extracted, each evaluated using the central 15 mm. Between the profiles a spacing of 1.57 µm is present. (c) ARS light scattering measurement: Scattered light distributions were recorded at 1250 positions along 50 profiles of 20 mm length each.

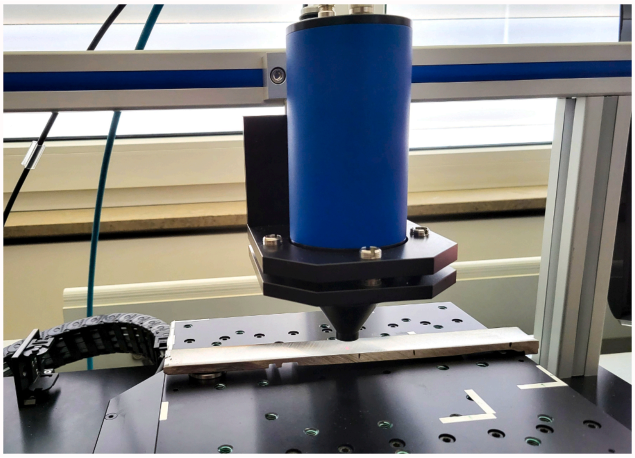

Fig. 3. Scattering light measurement – OS500 scanning one of the cylinder liners on an x–y table. [59].

(b) For the evaluation of the areal topography datasets obtained from the confocal microscope, the 400 central profiles were extracted and evaluated individually to achieve an identical data format as for the tactile measurements. Non-measured points within these profiles were interpolated. Even though each profile exceeded 15 mm in length, only one evaluation segment per profile was available. Subsequently, the same preprocessing steps (i–iv) as described in the previous section were applied to ensure consistent determination of the profile surface texture parameters and their statistical distribution.

(c) The ARS light distribution was recorded as intensity values along the photodetector for all 62,500 measurement points per sample. Each intensity distribution was normalized individually to transform the physically measured reflectance data into a mathematical angle distribution $I(\varphi')$ as a function of the angle φ'. This normalization effectively compensates for sample-specific material influences. In accordance with VDA 2009 [61], the following parameters were derived from the ARS light distributions to characterize various surface properties within the illuminated area: The $M-$value which represents the average gradient within the lightspot is a macroscopic property that is calculated as the center of gravity of the normalized intensity distribution $H(\varphi')$ and is directly connected to the macroscopic surface inclination angle α [61]:

$$\alpha\ tan\left(\frac{M}{2}\right),\ I = \sum I(\varphi') \tag{1}$$

$$M = \sum \varphi' H(\varphi'),\ H(\varphi') = \frac{I(\varphi')}{\sum I(\varphi')}$$

To characterize the micro-geometric characteristics, i.e. roughness, the stochastic moments of the angular distribution defined by VDA 2009 were evaluated, more particularly the variance A_q, skewness A_{sk} and kurtosis A_{ku} of ARS light distribution [61]:

$$A_q = k\sum(\varphi' - M)^2 H(\varphi'), \tag{2}$$

$$A_{sk} = \left(\frac{k}{Aq}\right)^{\frac{3}{2}} \sum(\varphi' - M)^3 H(\varphi'),$$

$$A_{\mathrm{ku}} = \left(\frac{k}{Aq}\right)^{2} \sum (\varphi' - M)^{4} H(\varphi').$$

The correction factor k is used for the normalization and ensures that a rectangular distribution within the angle range between the minimum angle $-\alpha$ and the maximum angle $+\alpha$ equals to a value of $A_{\mathrm{q}} = 100$. For industrial applications, M is often used to determine the macroscopic angle and A_{q} as a measure for the roughness within the light spot.

3.4. Analysis of height and angular distributions

In addition to the standardized surface parameters, the entire distributions of surface heights and surface angles were analyzed. The distribution of surface heights forms the starting point for many texture parameters, while the angular distribution can be derived from numerical differentiation of the topography according to ISO 21920-2 [12]. This allows a direct comparison between angular distributions obtained by ARS sensors and conventional surface texture measuring instruments. The combination of these two sets of variables enables a phase-space interpretation of the surface as proposed in [62]. Each sampling point is characterized by a generalized coordinate q_i (surface height) and a generalized velocity $\dot{q}_i$ (local slope or angle obtained from finite differences). The ensemble of pairs $(q_i, \dot{q}_i)$ defines a topographic state in a phase-space $\zeta(q,p)$. On this phase-space an energy-like state functional that separates a load-dependent configurational term B from a fluctuation term related to the angular statistics $\langle K\rangle$ can be defined. Formally, this can be expressed as [62]:

$$B = \xi \sum_{i=1}^{N} q_i \Delta x, \langle K\rangle = \frac{1}{N-1} \sum_{i=1}^{N-1} \frac{1}{2} m \dot{q}_i^{\,2} \tag{3}$$

where N is the number of sampling points and Δx the lateral sampling interval. The parameter ξ denotes the applied load or nominal contact pressure and m is a topographic scaling parameter chosen such that $\langle K\rangle$ has the same physical units as B. In this interpretation,

- B acts as a configurational contribution, capturing how the external load populates the height levels of the surface,
- $\langle K\rangle$ acts as a fluctuation contribution, encoding the variance of local slopes and thus the “activity” of the roughness.

Treating the surface topography as a two-dimensional subsystem of the bulk, an effective internal energy of the topographic ensemble is defined as [62]:

$$U_T = \langle K\rangle - B \tag{4}$$

Since the number of sampling points (or asperities) is fixed for a given measurement, not any particle-number term in the energy balance is introduced. Instead, the relevant additional state variable of the rough surface is the void volume V_{void} provided by the roughness, i.e. the geometrically defined volume of the valleys that remains available for material or lubricant to be displaced into. In practice, V_{void} can be obtained from the height distribution as the complement of the bearing volume at a given material ratio.

The conjugate generalized force to this void volume is the externally applied pressure ξ, so that the mechanical work associated with closing the multiscale voids of the roughness can be written as

$$\delta W = -\xi\, \mathrm{d}V_{\mathrm{void}}. \tag{5}$$

Formally, the differential of the effective internal energy of the topographic subsystem can therefore be expressed as

$$\mathrm{d}U = T_{\mathrm{eff}}\, \mathrm{d}S - \xi\, \mathrm{d}V_{\mathrm{void}}, \tag{6}$$

where S is an entropy measure of the phase-space occupation of height and angle states, and T_{eff} is an entropic temperature defined from the statistics of local slopes (for example via a maximum-entropy argument) rather than from molecular kinetic energy.

With these definitions, the generalized coordinates q_i and generalized velocities $\dot{q}_i$ naturally enter a Lagrangian-type functional of the surface state, which is used as a compact representation of the balance between fluctuation and configurational contributions in the topographic ensemble. Differentiation of L_T with respect to the generalized velocities yields a generalized momentum field

$$p_i = \frac{\partial L_T}{\partial \dot{q}_i} = m\, \dot{q}_i, \tag{7}$$

and thus an energy-like state functional [62]:

$$\frac{d}{d\dot{q}_i} L_T = \frac{1}{N} \sum_{i=1}^{N-1} m \dot{q}_i = \frac{1}{N} \sum_{i=1}^{N-1} p_i \tag{8}$$

leading to a Hamiltonian function [62]:

$$H(p,q) = p_i \dot{q}_i - U_T = \langle K\rangle + B \tag{9}$$

Each coordinate ζ_i of the surface ensemble therefore occupies a well-defined state in phase-space $\zeta(q,p)$ through its vertical displacement and its gradient. This phase-space representation combines the information from height and angular distributions in a single framework and provides a basis for linking topography-dependent state variables such as U, S, and V_{void} to tribological performance. Since this phase-space representation of a surface considers both the height and angular distribution, it allows for a comprehensive analysis and combines different perspectives on the surface that may lead to additional information for example regarding the description of tribological processes. The evaluation and comparison of both height distributions and angular distributions is implemented as additional analysis just as well as the phase-space plot showing the probabilities of the variable $\zeta(q,p)$.

4. Results

4.1. Topography measurements

Using the methodology described in Section 3, the topography of all 15 cylinder liners was measured by different measuring principles. The resulting areal topographies measured by the Confocal Microscope (CM) are shown in Figs. 4 and 5, which illustrate that the different cylinder liners, even though they feature the same application, have surface topographies with very different characters. The examined surfaces are typical examples for surfaces that are subject to high functional requirements e.g. regarding their tribological behavior.

The plots show the raw areal topography data of the 400 extracted profiles –after areal alignment and without any further processing. A visual comparison of these datasets highlights notable differences in both height ranges and surface structure types. Many cylinder liners exhibit the characteristic crossed groove patterns typical of the commonly used honing process, while others, such as cylinder liner 1, display more pronounced dales. These observations underscore the complexity of the surface topographies, which are subject to high functional demands in their respective applications. The comparison reveals that some cylinder liners, such as numbers 1, 8, and 9, exhibit a plateau-like stratified structure, while others – like CL 3 and 5 – display a highly irregular profile. The largest amount of non-measured points in the CM data was observed for CL 8 with a ratio of 0.28 %. Additionally, certain CLs, such as number 4, incorporate embedded particle structures. The scale and frequency of the groove features also vary considerably across the different profiles.

In addition to the areal plots, one representative evaluation position of both the CM and the stylus instrument (SI) is shown after the preprocessing – meaning as described in 3.3 the evaluation area has been filtered, aligned and cropped, resulting in the R-profile as defined in ISO

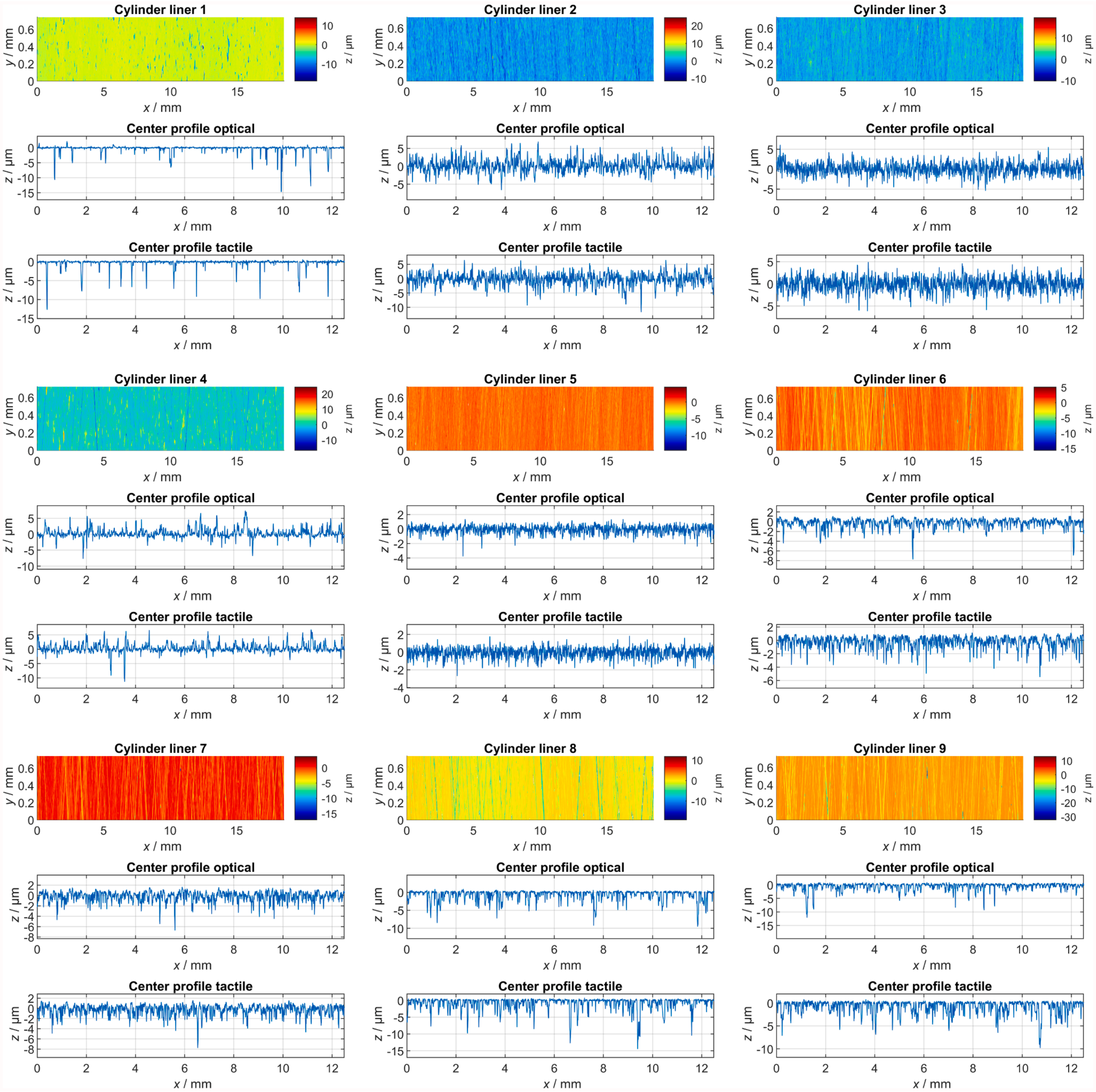

Fig. 4. Measured surface topographies of cylinder liners 1–9 – areal topographies measured by the confocal microscope, one exemplary profile of the areal dataset (evaluation area of profile 200 of 400) and one exemplary evaluation position of the tactile data (third evaluation position of profile 13 of 25).

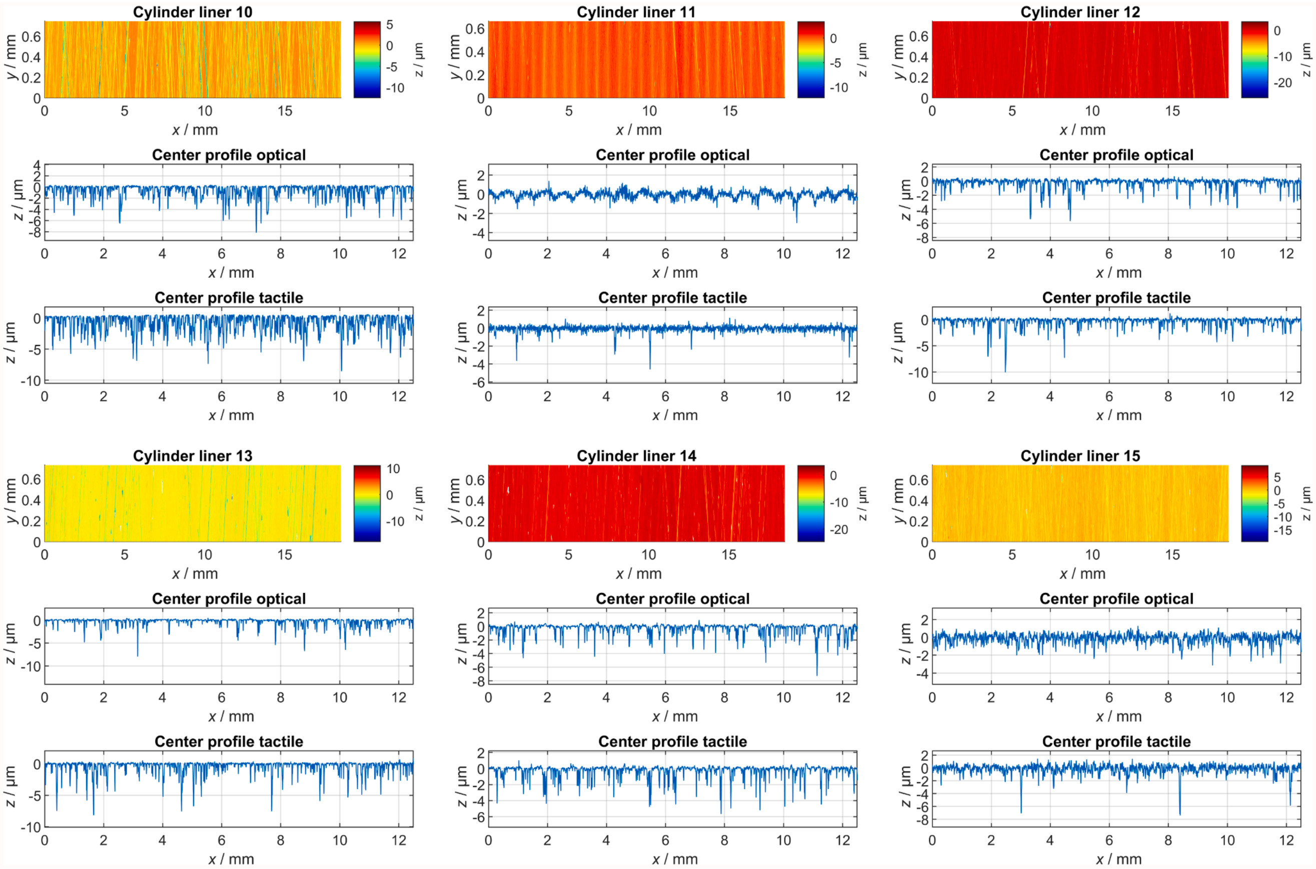

Fig. 5. Measured surface topographies of cylinder liners 10–15 – areal topographies measured by the confocal microscope, one exemplary profile of the areal dataset (evaluation area of profile 200 of 400) and one exemplary evaluation position of the tactile data (third evaluation position of profile 13 of 25).

21920-2. For the CM, the profile is shown as the evaluation area of the central profile, i.e. the profile with the index 200 of 400. For the SI, the profile of the 63rd evaluation is shown, i.e. the third evaluation position of profile 13 of 25. Fig. 4 summarizes the results for CLs 1–9, Fig. 5 the same results for the CLs 10–15. In the visual comparison of the tactile measured and optically measured profiles it can be observed that the surfaces have the same character, for some optically measured profiles e.g. CL 5 and CL 6 it seems like the short wavelength roughness is less pronounced than in the tactile data. Additionally for CL 11, there is a long-wave component in the optically measured profile that is possibly an artefact of the stitching process. Other than that, qualitatively, the data from the two measuring principles seem comparable, even though only one representative profile of each is displayed. To have a more comprehensive insight into the character of the measured surface topographies, subsequently a quantitative comparison of surface texture parameters under the consideration of all evaluation positions is described.

4.2. Surface texture parameters and angular parameters

After the described pre-processing, the profile surface texture parameters in accordance with the latest standardization of ISO 21920-2 were determined. Based on the measured areas that represent a statistically representative subset of the entire surface topography, in case of the optical measurement 400 parameter values each and for the tactile measurement 125 parameter values each were determined. With this evaluation it can be ensured that many surface height values are considered leading to a representative assessment of each component. The statistical distribution of the resulting surface texture parameters is visualized using violin plots. All 95 % confidence intervals based on the statistical distribution of all results can be found numerically in Appendix A.

Fig. 6 shows the distribution of the amplitude-based surface texture parameters for both the optical and tactile profile evaluation of CL 1–15. The numerical values can be found in Table 1 in Appendix A. When the distributions of R_a values are examined, it can be observed that there are some cylinder liners where the parameter distribution agrees very well, whereas for other cylinder liners there are major differences. One explanation for this is the fact that certain structures are transferred differently by the different measurement principles, meaning that the combination of wavelength, amplitude, and slope can cause different instrument responses and also a different degree of measurement uncertainty or artefacts in the data. Some reasons for differences can be found and explained by the metrological characteristics, e.g. a difference in the noise level, resolution capabilities or a different extent of artefacts in the data resulting in an instrument-specific topographic uncertainty. In most scenarios the tactile measurement features systematically larger values just as well as a larger scattering of the parameter values. This scattering, however, cannot be assigned to the measurement uncertainty but to a vast majority is connected to the statistics of the surface since the distribution of all measured values is shaped by the different evaluation positions and not a repetition of the measurement. Since in many

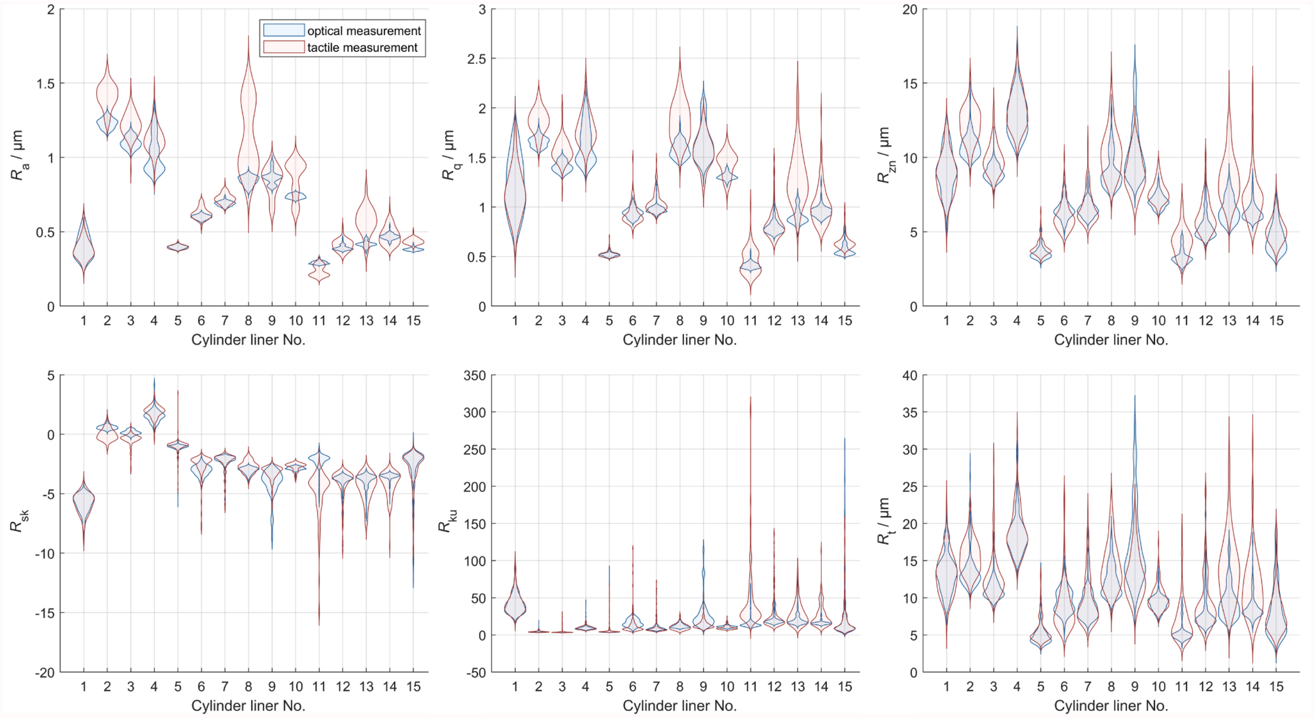

Fig. 6. Violin plot of the distribution of profile surface texture parameters. The distribution of all 400 evaluated profiles (optical) and 125 evaluated profiles (tactile) are shown for the cylinder liners 1–15. The amplitude-based parameters R_a, R_q, R_{sk}, R_{ku}, R_t and attribute parameters based on peak heights and pit depths R_z are displayed.

cylinder liners there are very distinct features that can significantly influence the amplitude-based parameters there is a major scattering of the values when different profiles are evaluated at different positions. These statistics of the surface for example can lead to a value range in the measurements of cylinder liner 8 between 0.5 and 1.8 µm R_a. This example shows the significant influence of these statistics of the surface or more particularly the position of measurement and evaluation. The effects of the statistics of a surface were e.g. described by Seewig [63]. The numerical values in the Appendix also show that the influence of this effect is mostly larger than the systematic differences between the two measuring principles.

The fact that the optical results scatter less pronounced in many cases can lead to the assumption that some short wavelength features that accord for a variation of the average roughness values are not transmitted as pronounced as for the tactile measurement. The results of the arithmetic mean height R_a and the root mean square height R_q are similar even though for R_q also more scattering of the optical results can be observed. When the maximum height R_z is evaluated (labelled as R_{zn} to highlight that the latest definition of ISO 21920-2 was used), the results of the two measuring principles are much more comparable meaning that the overall measured amplitude distribution of the extreme values is similar. The results indicate that the R_z parameter is inherently sensitive to the evaluation position and scatters due to the statistical characteristics of the surface. Consequently, it can exhibit substantial variability, such as ranging from approximately 4 µm to 14 µm for CL 1.This observation again confirms that an R_z value does not allow a representative characterization of a surface especially not regarding its functional or tribological behavior. The same observation can be made for the total height R_t. For the analysis of the skewness R_{sk} there are also some surfaces where differences between the different methods can be observed which shows that there may be variations in the transmission behavior regarding either hills or dales when certain features occur. For the kurtosis R_{ku} the largest scattering of the parameter values can be observed. Since extreme values contribute to the power of four, outliers or artefacts in the data can significantly change the result and for some cylinder liners a broad variation of the value can be observed. Overall, the results of the amplitude-based parameters show that in some scenarios similarities between the different amplitude distributions can occur – however there are also differences between the optical and tactile results that should be explored further.

Fig. 7 shows the same visualization of results for the hybrid parameters that are based on an angular evaluation. The results can also be found in Table 2 in Appendix A. The slopes and curvatures were evaluated based on the numerical differentiation defined in ISO 21920-2. In the angular-based evaluation, large differences between the two datasets can be exposed. This is explainable since based on the numerical differentiation possible uncertainties are amplified resulting in a larger uncertainty of angular-based parameters when determined using height topography values. For the R_{dq} values it can be observed that the root mean square gradient of the optical surface topography data is systematically larger for all evaluated cylinder liners. The degree of difference depends on the character of the surface. One explanation for these are outliers or artefacts in the optically measured data that lead to a local increase of the surface gradient. For surfaces where a priori knowledge is present, e.g. material measures applied in calibration measurements, the removal of implausible points is possible based on the standardization [64], however remains challenging for practical engineering surfaces. For the maximum absolute gradient, i.e. R_{dt} value, which describes the

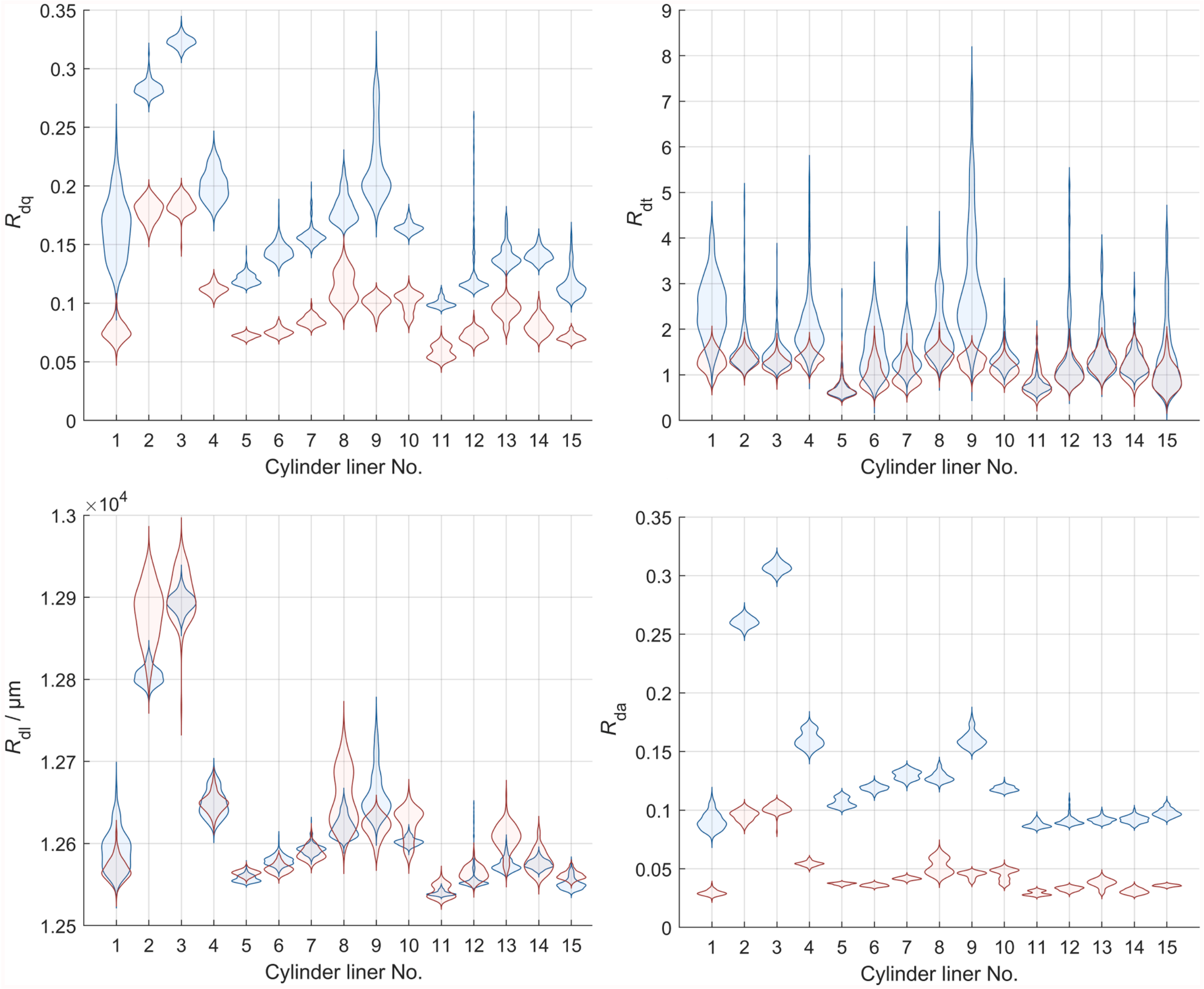

Fig. 7. Violin plot of the distribution of profile surface texture parameters. The distribution of all 400 evaluated profiles (optical) and 125 evaluated profiles (tactile) are shown for the cylinder liners 1–15. The hybrid parameters R_{dq}, R_{dt}, R_{dl}, R_{da} are displayed.

extreme value of the gradient, also systematically larger values tend to occur for the optical measurement. The same is also true for the arithmetic mean of the absolute gradient, the R_{da} value, whose results strongly correlate with R_{dq}. For the developed length R_{dl}, the difference between optical and tactile measurement is not as significant. Overall, it can however be exposed that the distribution of surface slopes and curvatures differs much more between the tactile and optical data than the distribution of the height values. This confirms the observation made in previous examinations that the variables are independent from each other [59]. A central objective of this study is to demonstrate that, although the results obtained by the two methods may differ, both approaches can enable reliable monitoring capabilities – particularly when angular and height parameters are combined and relative changes in these variables are monitored.

When the parameters based on profile elements and attribute parameters are examined as shown in Fig. 8, the following results can be obtained: Both the R_{sm} count (no. of profile elements) and the mean profile element spacing R_{sm} value are largely similar for the two measuring principles; only the width of the distributions for the optical and tactile measurements differs slightly in some cases. This shows that the lateral dimensions of the individual profile elements are not significantly influenced by the measurement principle. The same is also true for the values of the maximum profile element height R_{cmax}, maximum peak height R_{pmac} and maximum pit depth R_{vmax}. For the mean profile element height R_c some differences can be observed: in certain scenarios the tactile measurements feature larger values, in others the optical measurements – there is also no clear systematic trend. This shows that the examined group of parameters features overall similar results for both physical measuring principles. All results can also be found in Table 3 in Appendix A.

Another interesting group of parameters is examined in Fig. 9 – the function-oriented surface texture parameters for stratified surfaces, the core height R_k, reduced peak height R_{pk} and reduced pit depth R_{vk}. Their results can also be found in Table 4 in Appendix A. Since these parameters are commonly used in the assessment of tribological processes, they can provide meaningful insights into the functionality of a

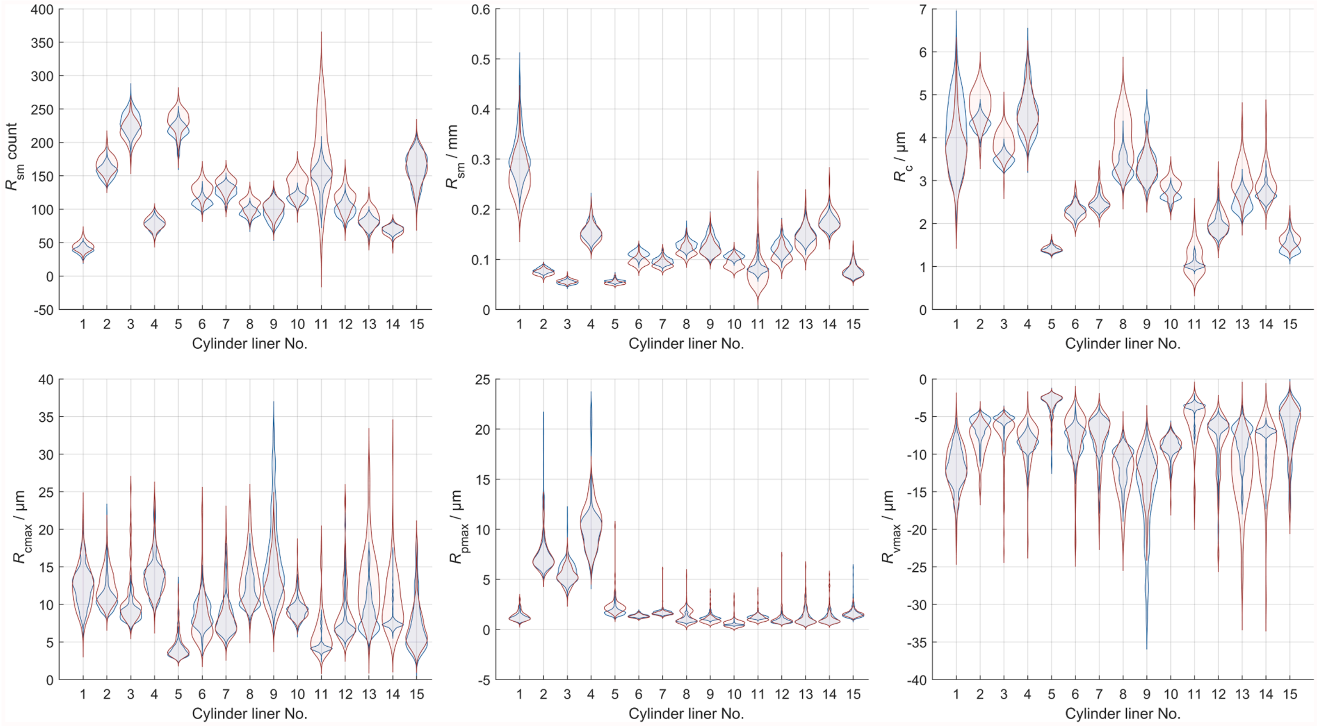

Fig. 8. Violin plot of the distribution of profile surface texture parameters. The distribution of all 400 evaluated profiles (optical) and 125 evaluated profiles (tactile) are shown for the cylinder liners 1–15. The parameters based on profile elements: R_{sm} *count* (no. of profile elements), R_{sm}, R_c, R_{cmax}, and the attribute parameters R_{pmax}, R_{vmax} are displayed.

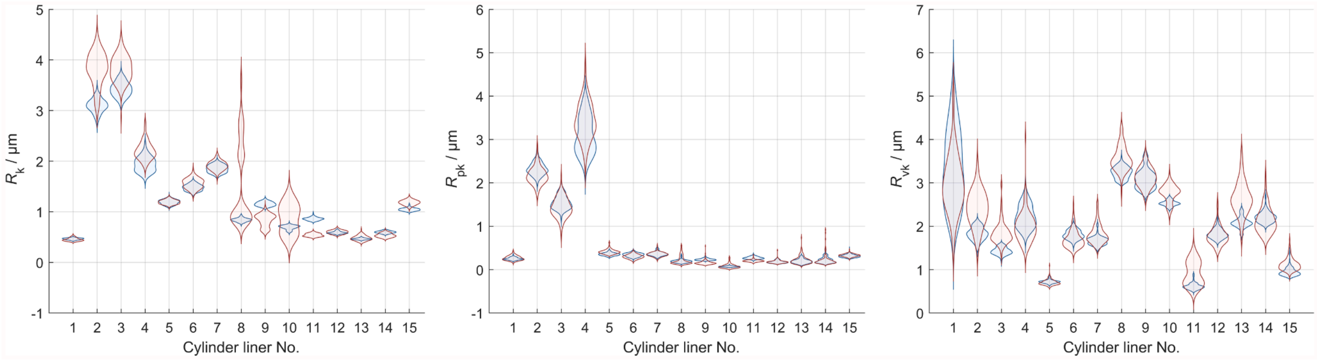

Fig. 9. Violin plot of the distribution of profile surface texture parameters. The distribution of all 400 evaluated profiles (optical) and 125 evaluated profiles (tactile) are shown for the cylinder liners 1–15. The parameters for stratified surfaces using the material ratio curve: R_k, R_{pk}, R_{vk} are displayed.

workpiece even though one of their limitations is the fact that they are also solely based on the height distribution. Similarly to the examination of the amplitude-based parameters for the core roughness depth R_k it can be observed that for some surfaces the tactile measurement leads to larger values. Just the same observation can also be made for R_{vk}. This is an agreement to previous observations where it was shown that deep and wide dales could be scanned more accordingly using tactile measuring instruments [37]. For R_{pk} there is a better agreement of the parameter distributions. This again supports the hypothesis that the transfer behavior of hills and dales is influenced by different physical effects of the applied measuring instruments. Overall, however, there is no major difference between the two sets of parameters and most of the distributions overlap. This illustrates that the height distributions are in a better agreement than the angular distributions and that the statistics of the surface is more significant for the parameter values than the systematic influences of the measuring instruments.

To further examine this aspect, a comparison of mean peak height R_p and mean pit depth R_v is shown in Fig. 10. The results can also be found in Table 5 in Appendix A. In this analysis, the dales are the most significant features for many of the examined cylinder liners and the wide scattering of the R_v values throughout the evaluations demonstrates that distinct features are present. It can also be confirmed that the R_p values agree better between the different measuring principles than the R_v values. This shows that the differences that are given in the set of measured height values are mostly linked to the transmission of dales whereas the measurement of hills is in better agreement between the optical and tactile measurements.

As a last parameter evaluation, also the measurements of the angular-resolved scattering light sensor are considered. The distribution of the variance, skewness and kurtosis of the angular distributions is summarized in Fig. 11. The results can also be found in Table 6 in Appendix A. Here, also the distributions of the parameters for the two lightspot sizes are compared. Again, a significant impact of the statistics of the surface – meaning the effect of the evaluation position – can be

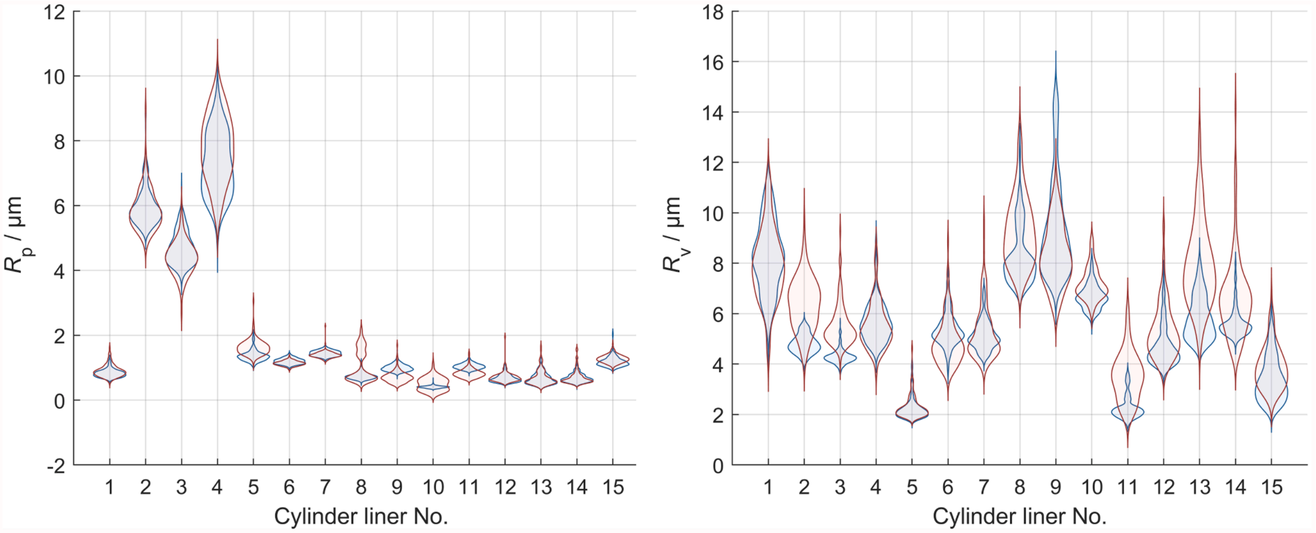

Fig. 10. Violin plot of the distribution of profile surface texture parameters. The distribution of all 400 evaluated profiles (optical) and 125 evaluated profiles (tactile) are shown for the cylinder liners 1–15. The attribute parameters based on peak heights and pit depths: R_p, R_v are displayed.

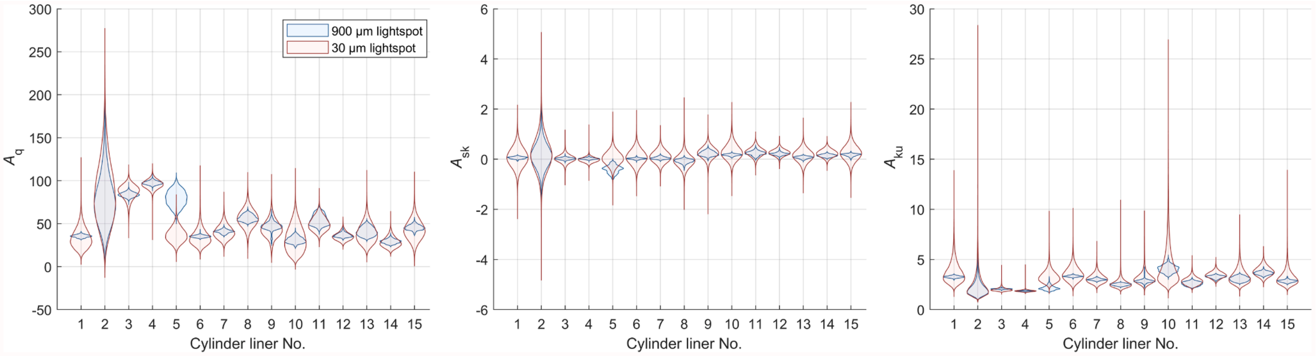

Fig. 11. Violin plot of the distribution of angular ARS light parameters. The distribution of all 62,500 evaluation positions per cylinder liner are shown for the 900 µm lightspot and 30 µm lightspot each. The statistical moments variance, skewness and kurtosis of the angular distribution A_q, A_{sk}, A_{ku} are shown.

observed. For some cylinder liners the effect is more pronounced than for others. The absolute value of for example the variance of the angles A_q varies for the different cylinder liners showing the different degree of roughness. The measurements of the two lightspot sizes are mostly in good agreement. However, there are also some exceptions like for example CL5. The different results for the two lightspot diameters show that in this surface a larger extent of short wavelengths roughness is present that is filtered by the larger lightspot. Otherwise, the systematic results for the skewness A_{sk} and kurtosis A_{ku} are mostly similar for both light spot diameters. It can however be observed that in most scenarios the values for the smaller lightspots scatter more significantly. This can be explained by the extraction of a smaller sample size of the surface leading to a larger influence of the statistics of the surface.

When in a previous study, surface texture parameters and the angular parameters of the angular-resolved scattering light sensor were compared, it could be shown that there were strong correlations between certain parameter sets whereas others did not exhibit a correlation at all [59]. Based on this the conclusion was drawn that the two sets of information height distribution and the directly measured angular distribution provide a comprehensive set of information [59]. To further explore this, subsequently the different height and angular distributions of the various measuring principles are compared.

4.3. Height and angular distributions

4.3.1. Height distributions

Since it was shown that the parameters that are based on the height values feature different properties than the ones based on the angular distribution, the height and angular distributions are evaluated comprehensively. For this process the frequency band of the height data was adjusted with regard to the angular scattering light sensor to allow a direct comparison. Based on the transfer behavior of the ARS sensor, a nesting index of $N_{iL} = 1.285mm$ was used assuming the lightspot diameter of 900 µm and the transfer behavior as described by Seewig et al. [56]. This means that a profile-based filtering using the robust Gaussian filter as L-Filter with $N_{iL} = 1.285mm$ was applied. As S-Filter, the linear Gaussian filter was used to remove the instrument specific characteristics from the data with a nesting index of $N_{is} = 2.5\mu m$. The resulting height distributions of all optical and tactile height topography data are summarized in Figs. 12 and 13. In the direct comparison, it can be verified that the qualitative distribution of height values is similar for both measuring principles. Also, the optical measurements feature a higher peak in probability around the height of zero – explaining the mostly smaller R_a-values in comparison to the tactile measurements. Generally, however the distributions of height values have a similar shape and no significant systematic differences in the transfer behavior can be inferred based on the plots.

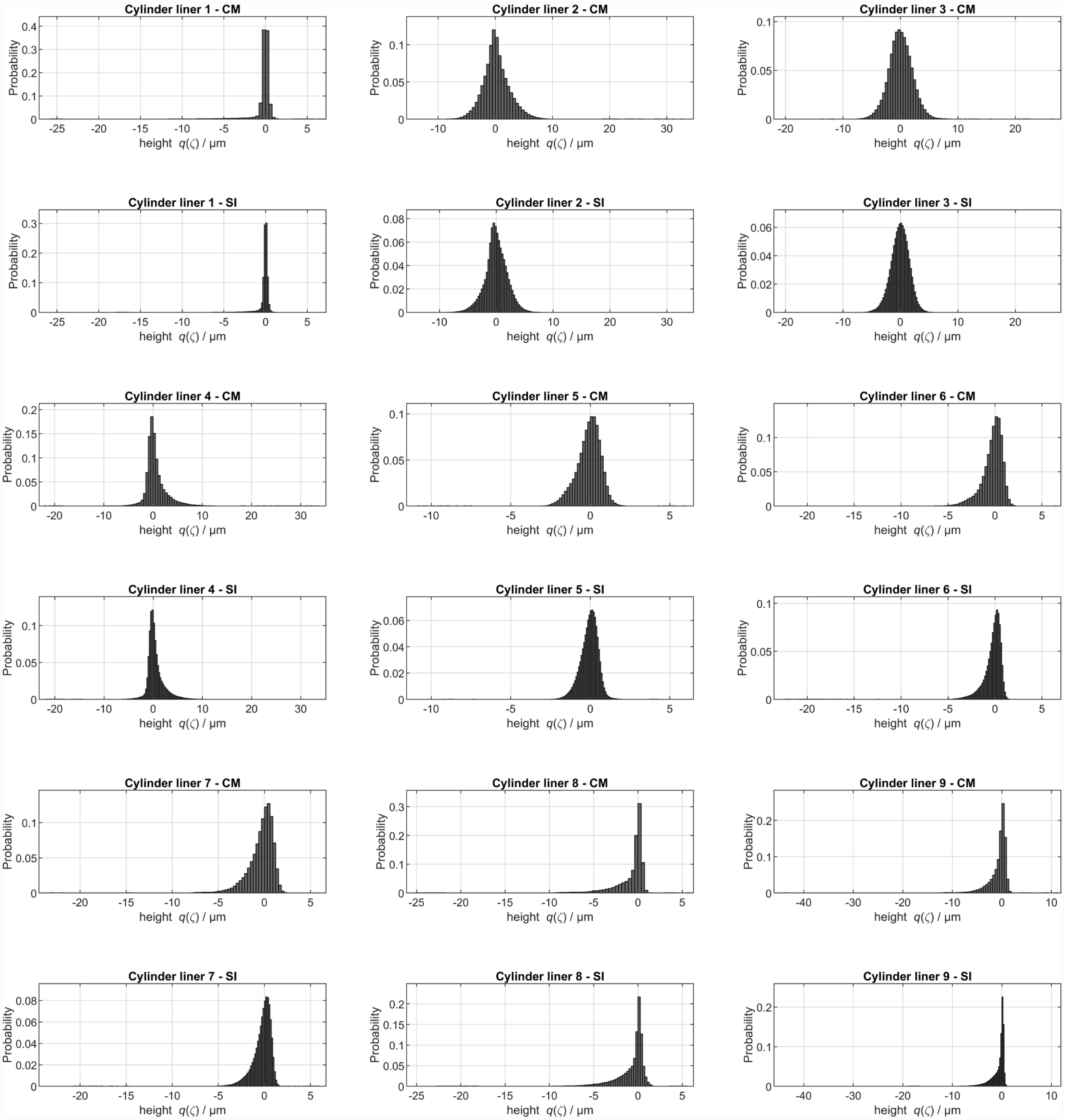

Fig. 12. Height distributions of all optical confocal microscope (CM) and tactile stylus instrument (SI) height topography data. The topography data was processed profile-wise with a linear S-filtering (ISO 16610–21) $N_{is} = 2.5\mu m$, a subtraction of a fitted least squares straight line and L-filtering with a robust Gaussian filter of second order (ISO 16610-31), $N_{iL} = 1.285mm$. The data of cylinder liners 1–9 is summarized.

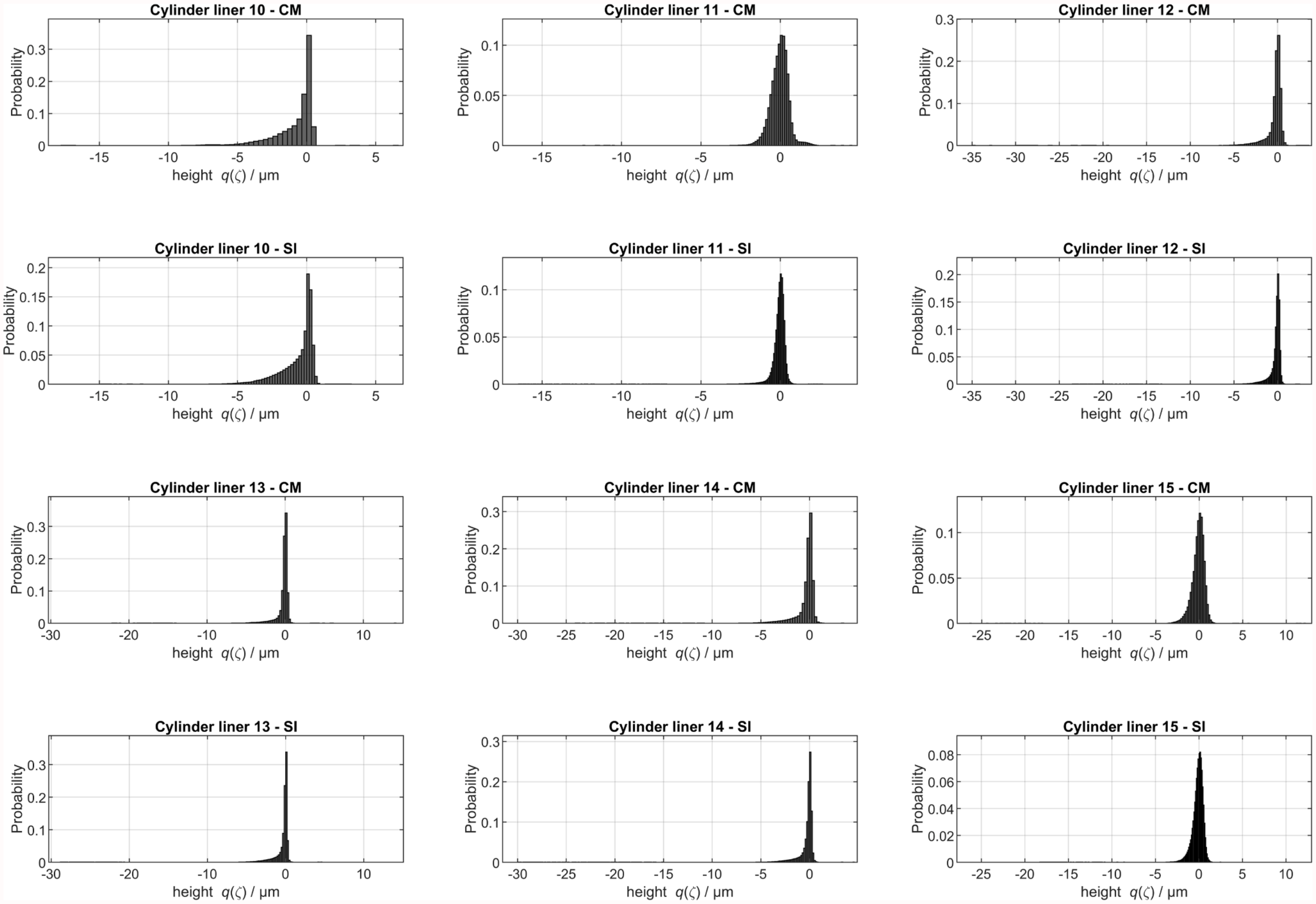

Fig. 13. Height distributions of all optical confocal microscope (CM) and tactile stylus instrument (SI). The topography data was processed profile-wise with a linear S-filtering (ISO 16610-21) $N_{is} = 2.5\mu m$, a subtraction of a fitted least squares straight line and L-filtering with a robust Gaussian filter of second order (ISO 16610-31), $N_{iL} = 1.285mm$. The data of cylinder liners 10–15 is summarized.

4.3.2. *Angular distributions*

When the angular distributions of the same evaluated profiles are compared, for CL 1–3 the distributions in Fig. 14 result. Fig. 15 shows the same results for CL 4–6, Fig. 16 for CL 7–9 whereas all remaining results can be found in Appendix B (Figs. 20 and 21). The angles of the measured height topographies were determined using the numerical differentiation described in ISO 21920-2. When the four different measured distributions per cylinder liner are compared with each other, clear differences can be observed. The ARS sensor allows a direct measurement of the angular distribution without numerical differentiation of the surface topography that can significantly increase the present measurement uncertainties. For many surfaces the angular distributions of the optical and tactile measurement differ significantly. This confirms the previous observation within for example the R_{dq} comparison and shows that the height and angular distributions of a surface should be interpreted as independent variables that provide two different perspectives on the character and functionality of a surface.

For many surfaces e.g. CL 1 or 6, a good agreement between the stylus instrument (SI) and the ARS sensor can be achieved. The confocal microscope (CM) features a larger scattering of the angles and measures a larger probability of higher angular values than the SI. The angular-resolved scattering light sensor (ARS) sensor features a measurement range which is limited to ±16° which can be a limitation for some very rough surfaces, e.g. CLs 2 and 3. For CL2 also an insufficient reflectivity can be assumed resulting in a significant scattering of the ARS results. For the results of CL 7–9, which can be found in Fig. 16, the better agreement between the tactile data and the directly measured angular distribution can also be clearly observed. Similarly, the results of CL 10–15 in the Appendix confirm this effect. The conclusion can be drawn that the larger scattering of angles in the optically measured height data just as well as the occurrence of larger surface angles can be explained by instrument specific effects or measurement artefacts. Because of the better agreement between the SI and the ARS sensor it can be concluded that this measurement principle provides better insights into the angular distribution. For example, when CL 7 or 9 are considered, the CM distribution features a notably larger scattering of the angular distribution.

4.4. *Phase-space representation*

Already in previous studies it was observed that the height distribution and angular distribution provide different insights into the character or functionality of a surface. This was confirmed in the present study where the height distributions and angular distributions feature very different degrees of comparability between different measuring

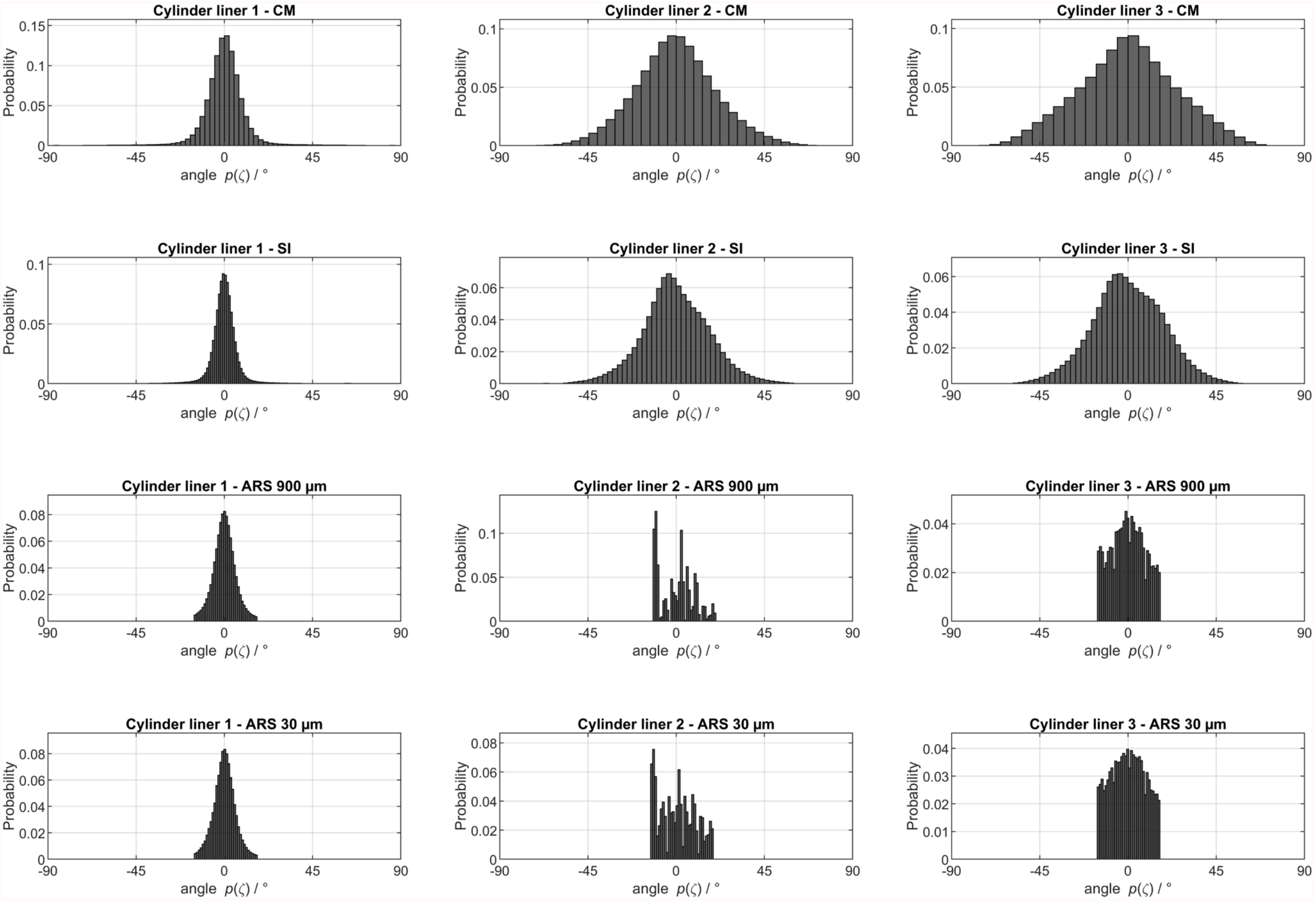

Fig. 14. Angular distributions of all optical confocal microscope (CM), tactile stylus instrument (SI) and angular-resolved scattering light measurement (ARS) data. The topography data was processed profile-wise with a linear S-filtering (ISO 16610-21) $N_{is} = 2.5\mu m$, a subtraction of a fitted least squares straight line and L-filtering with a robust Gaussian filter of second order (ISO 16610-31), $N_{iL} = 1.285mm$. Additionally, the directly measured angular distributions using the ARS light sensor featuring lightspot diameters of 900 μm and 30 μm are shown. The data of cylinder liners 1–3 is summarized.

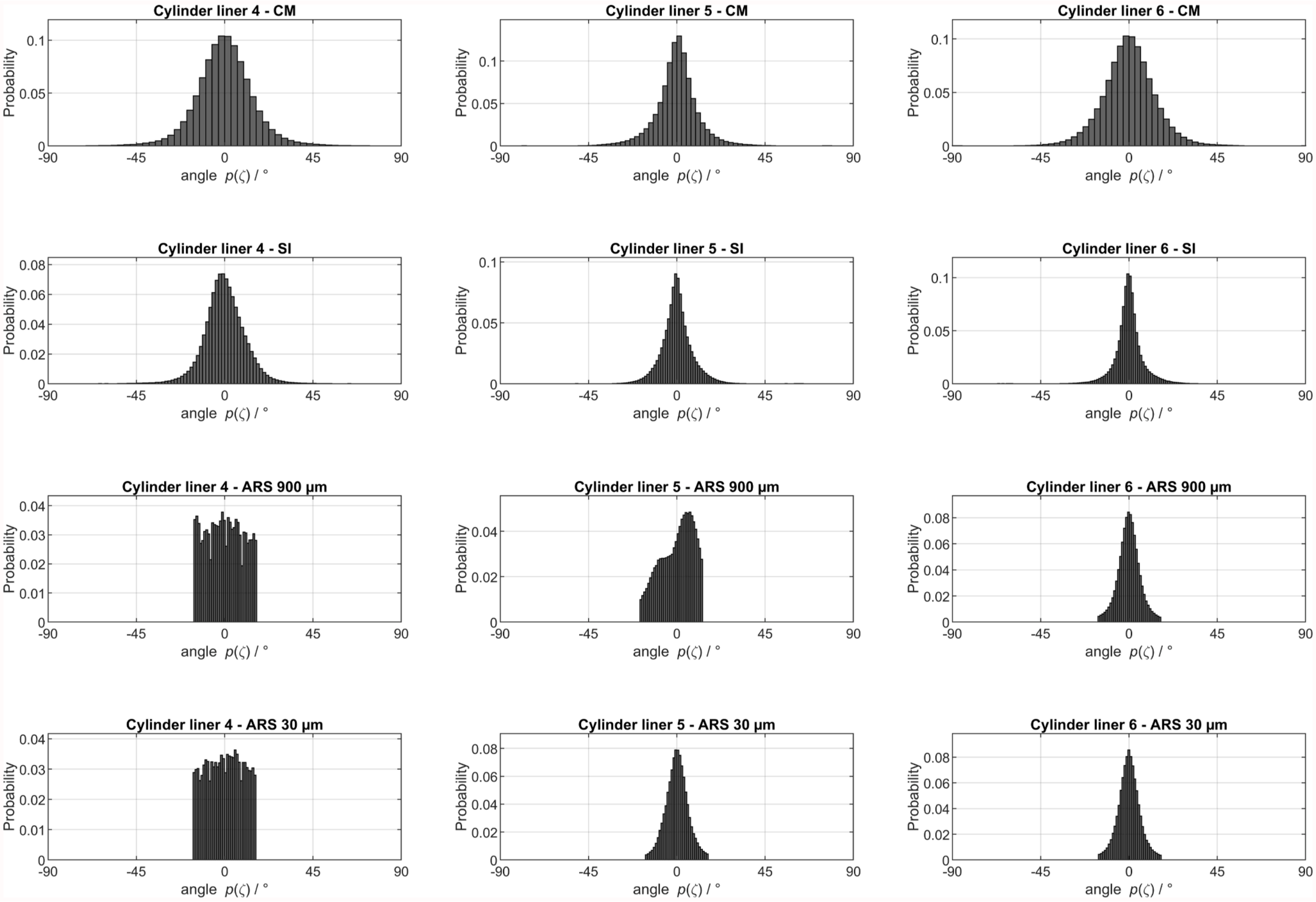

Fig. 15. Angular distributions of all optical confocal microscope (CM), tactile stylus instrument (SI) and angular-resolved scattering light measurement (ARS) data. The topography data was processed profile-wise with a linear S-filtering (ISO 16610-21) $N_{is} = 2.5\mu m$, a subtraction of a fitted least squares straight line and L-filtering with a robust Gaussian filter of second order (ISO 16610-31), $N_{iL} = 1.285mm$. Additionally, the directly measured angular distributions using the ARS light sensor featuring lightspot diameters of 900 µm and 30 µm are shown. The data of cylinder liners 4–6 is summarized.

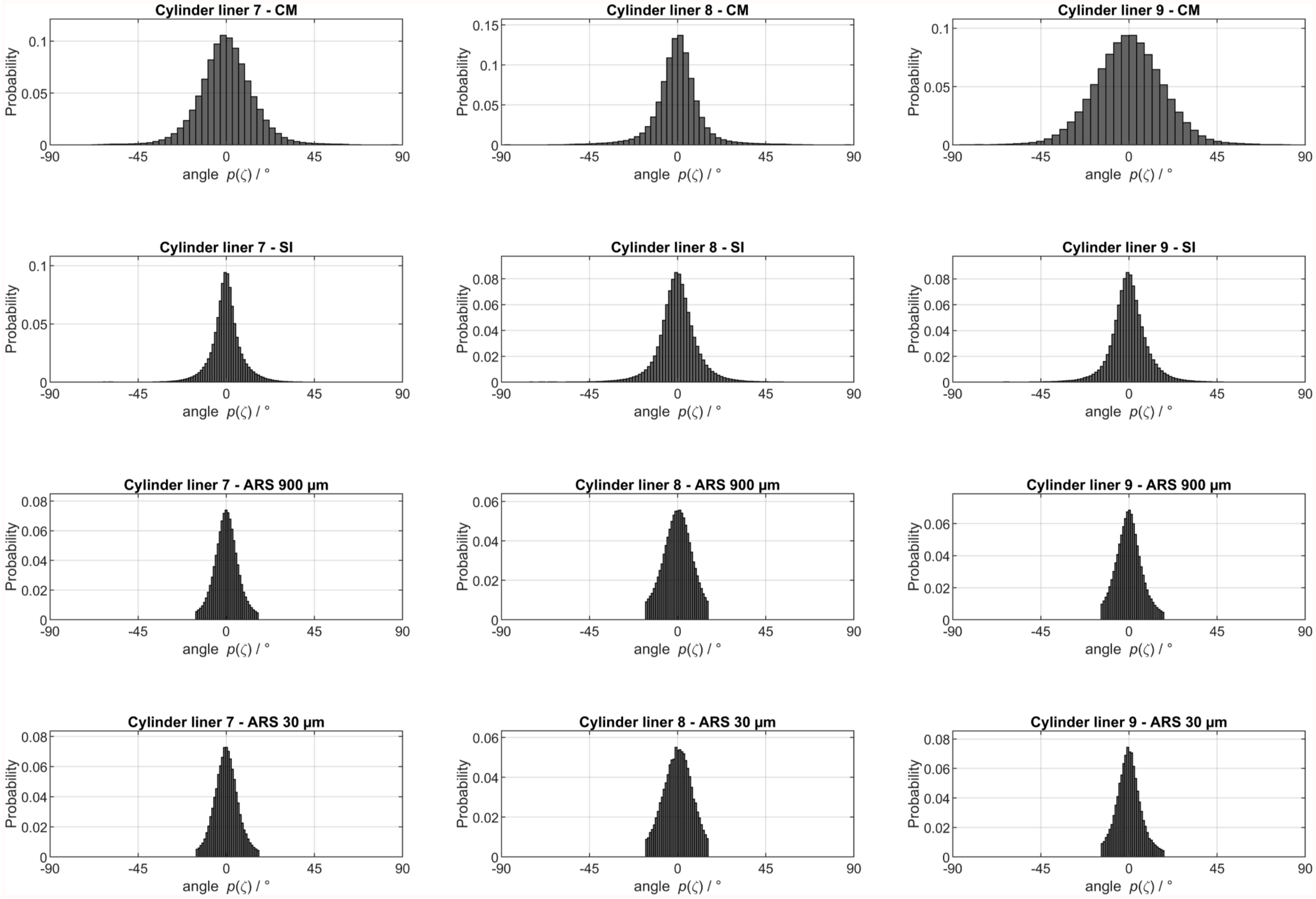

Fig. 16. Angular distributions of all optical confocal microscope (CM), tactile stylus instrument (SI) and angular-resolved scattering light measurement (ARS) data. The topography data was processed profile-wise with a linear S-filtering (ISO 16610-21) $N_{is} = 2.5\mu m$, a subtraction of a fitted least squares straight line and L-filtering with a robust Gaussian filter of second order (ISO 16610-31), $N_{iL} = 1.285mm$. Additionally, the directly measured angular distributions using the ARS light sensor featuring lightspot diameters of 900 µm and 30 µm are shown. The data of cylinder liners 7–9 is summarized.

principles. Thus, their combination can provide a more comprehensive view on a workpiece than just having a look at one of those variables which leads to the described phase-space representation of a surface as previously derived in [62]. In this representation, the distribution of heights and angles, which represent the first derivative of the surface topography, are mapped in an *x*-*y*-diagram. These two variables are imaged in coordinates *p* and *q*, and each coordinate ζ_i of a topography ensemble obtains now a defined position in the phase-space $\zeta(q,p)$. Each element ζ_i of a topography ensemble describes a defined position in the phase-space defined by its height q_i and its gradient p_i, i.e. $\zeta_i = \zeta(q_i, p_i)$ [62]. The statistical distribution of the different phase-space positions, references as classes, is illustrated using a discrete set of combinations and a corresponding discretization must be defined.

Since in general surface topography features fractal dimensions, no smooth manifold in the configuration space is given, but the definition of a smallest representable wavelength allows for a physically meaningful scale. To determine the differentials *dq* and *dp* of the two variables, the RMS values σ_q, σ_p of the ensemble $\boldsymbol{\zeta}_\mathbf{N}$, which corresponds to R_q in the roughness norm are considered for the variables $\mathbf{q} = \mathrm{q}_i, i = 1, \cdots, N \bullet M$, $\mathbf{p} = \mathrm{p}_i, i = 1, \cdots, N \bullet M$ when *M* profiles with *N* points each are considered:

$$\sigma_q = \sqrt{\langle \mathbf{q}^2 \rangle - \langle \mathbf{q} \rangle^2}, \sigma_p = \sqrt{\langle \mathbf{p}^2 \rangle - \langle \mathbf{p} \rangle^2} \tag{10}$$

To determine the class width *cw* of the height and angular axis, 'Scott's Rule' is used, which minimizes the integrated mean squared error (IMSE) for a sample size *N* with a standard deviation σ [65]:

$$cw_q = \frac{\varepsilon \sigma_q}{\sqrt[3]{N}}, cw_p = \frac{\varepsilon \sigma_p}{\sqrt[3]{N}} \tag{11}$$

ε represents a scaling factor with 3.49 for the normalized Gaussian distribution, σ_q the RMS-value of $q(\boldsymbol{\zeta}_\mathbf{N})$, and *N* the number of information bearing coordinates which is chosen as the number of points in one profile since this represents the statistical ensemble of one evaluation. The basic assumption for randomly rough surfaces is a normal distribution of heights values, so that ε is chosen as 3.49. The resulting class widths *cw* are determined both for the height values and the angle values, resulting in dq, dp. The probability of the plot is normalized.

The resulting phase-space representations map the relative probability of the occurrence of a value within a class $p_{rel}(c_q, c_p), c_q = \min(\mathbf{q}), \min(\mathbf{q}) + dp, \cdots, \max(\mathbf{q}), c_p = \min(\mathbf{p}), \min(\mathbf{p}) + dq, \cdots, \max(\mathbf{p})$ and the results of the cylinder liners are summarized in Fig. 17 for CL 1–6, whereas the remaining evaluations can be found in Appendix C (Figs. 22–24). When e.g. CL1 is considered, clear differences of the plots for the CM and SI can be identified, which based on the previous results can be mostly assigned to the differences in the angular distributions since it was shown that the surface texture parameters and the height distributions were often comparable. The phase-space plot also allows the visualization of even slight differences caused e.g. by optical artefacts that lead to large measured angles. For CL2 and 3, these results can be confirmed: even though the height distributions are very comparable for the optical and tactile measurement, based on the differences in the angular transmission, significant differences in the phase-space representation can be exposed. This is observed even though both

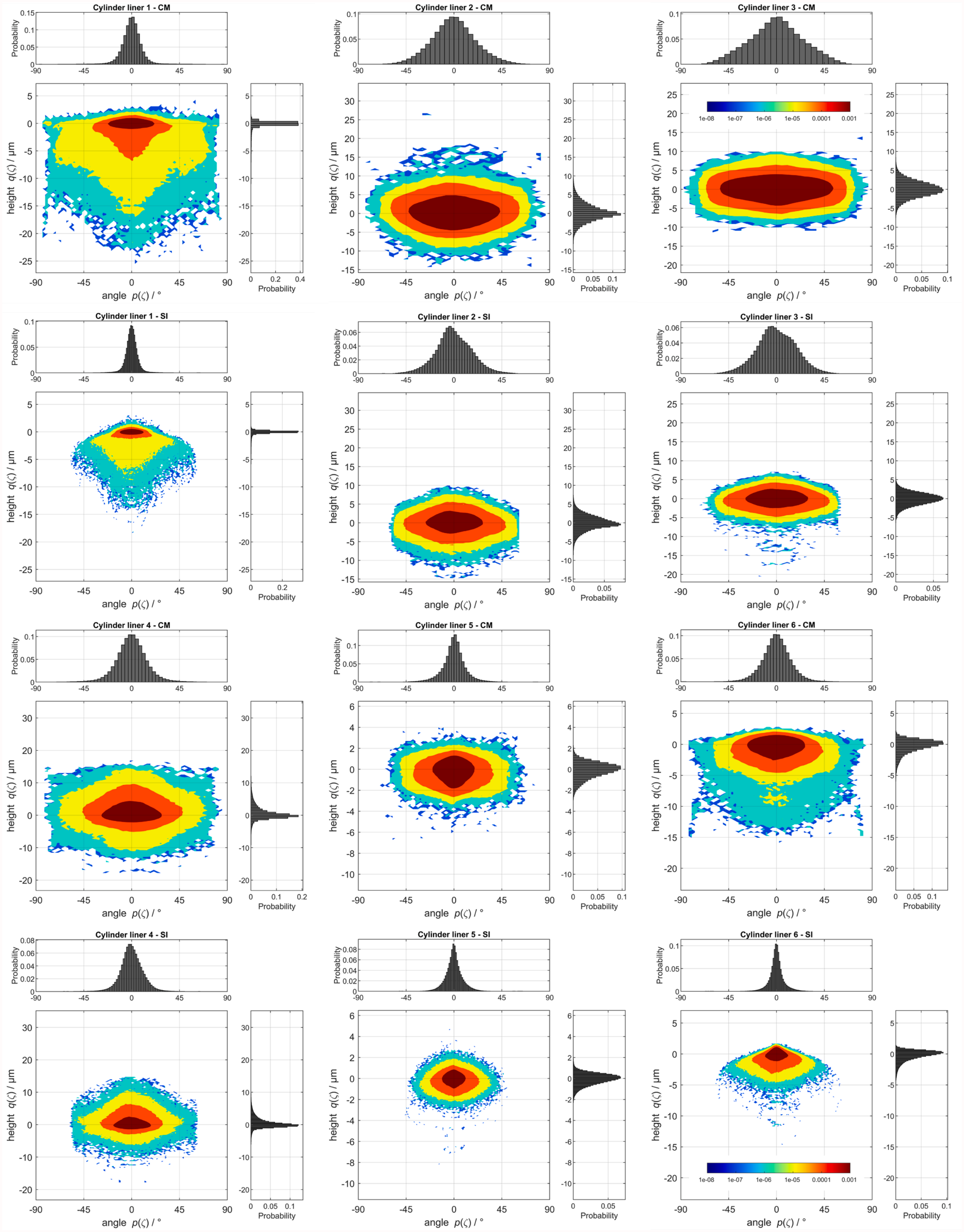

Fig. 17. Phase-space plot of all optical confocal microscope (CM), and tactile stylus instrument (SI) height topography data. The topography data was processed profile-wise with a linear S-filtering (ISO 16610-21) $N_{is} = 2.5\mu m$, a subtraction of a fitted least squares straight line and L-filtering with a robust Gaussian filter of second order (ISO 16610-31), $N_{iL} = 1.285 mm$. The data of cylinder liners 1–6 is summarized.

measurement approaches lead to similar surface texture parameters and also mostly to similar distribution of height values. Again, the impact of nonlinear transfer effects can be observed by the occurrence of larger angle values in the optically measured data. The fact that these values feature very small probability indicates that these values are strongly influenced by outliers in the data. These observations clearly demonstrate the differences between the transfer behavior of the two types of instruments. When the remaining cylinder liners are evaluated, these results can be achieved consistently. The phase-space diagram leads to an effective representation that can already expose smaller differences that cannot be uncovered using the distributions of either the angles or the heights or height-based surface texture parameters. When the surface texture parameters, including the function-oriented parameters like R_{k} and R_{pk} were compared, they could not expose the differences between transfer behaviors of the different measuring principles just as well as the impact of possible nonlinear effects. These examples prove that the phase-space representation provides a more comprehensive representation of the surface than just focusing on either height-based or angular-based parameters. For the assessment of tribological behavior of a surface, a more comprehensive view on the surface topography should be applied since also the angular distribution has a significant impact on the behavior of the surface.

Since the determination of an angular distribution based on a height measurement can lead to notable uncertainty, it is also explored to combine the directly measured angular information of the ARS sensor and the height distribution of the CM and SI measurements into a phase-space representation. In doing so, the probability of height values $h_i(q)$, $i = 1, 2, \cdots, N_q$ resulting from the surface height measurement and the probability of angular values $g_i(p), i = 1, 2, \cdots, N_p$ resulting from the ARS light measurement are combined as follows to a superposed phase-space representation:

$$\boldsymbol{H} = h \bigotimes 1_{N_p}, \boldsymbol{G} = 1_{N_q} \bigotimes g, \zeta = \boldsymbol{H}^{\circ} \boldsymbol{G} \tag{12}$$

Fig. 18 summarizes the results for CLs 1–3, the remaining results of CLs 4–15 can be found in Appendix D (Figs. 25–28). The results confirm again that the height distributions of the CM and SI measurements are much more comparable than the angular distribution. This can be inferred from the fact that the representations look much more comparable than before when the angular distributions calculated by the height measurements were used for the phase-space plots. The plots also illustrate that the lightspot diameter does not have a major influence on the results since the representations are very similar for both diameters. However, the wider scattering of the height axis that can be observed in many CM measurements again leads to some changes of the phase-based representation. These values can be assigned to outliers or artifacts in the data as described above. Generally, the results are much more comparable than when the angular distributions of the height measurements are used. This shows that the combination of a direct measurement of surface heights and angles can lead to a powerful and comprehensive visualization and representation of the surface topography which is already sensitive to small changes and thus allows has significant potential for the monitoring of tribological processes. Thus, it makes sense to combine the measurement of height topographies with the direct measurement of the angular distribution using ARS sensors.

A direct angular measurement allows a more reliable determination of the angular distribution in comparison to a numerical differentiation of the height topography. For some CLs, like CLs 2, 3 and 4, differences in the angular transmission of the ARS, SI and CM can be observed which originate from the large slopes in the height data and the filter effect of the topography measurement. For some ARS measurements an almost rectangular distribution of angles is measured. For other surfaces, like CLs 6, 7 and 10–15 a much better agreement of the angular transmission can be observed – also resulting in a good agreement between the different phase-space representations. This illustrates again the fact that the separate measurement of heights and angles provides a comprehensive perspective on the surface topography and the associated functional characteristics.

4.5. *Quantitative assessment of phase-space plots*

To compare the different phase-space representations, quantitative analysis was carried out. In doing so, the relative probability value of the individual classes of the phase-space plot was imaged as a function of the cumulative area A in the plot which is determined by the number of classes that occur with at least a certain probability p^*:

$$A\left(p^*\right) = cw_q cw_p \frac{\left|\left\{p_{rel,i} \in p_{rel}\left(c_q, c_p\right) \left|p_{rel,i} > p^*\right.\right\}\right|}{N_q N_p}, \tag{13}$$

In Appendix E, Tables 8 and 9, the results for $A\left(p^* = 10^{-3}\right), A\left(p^* = 10^{-4}\right), A\left(p^* = 10^{-5}\right), A\left(p^* = 10^{-6}\right)$ - meaning the areas within the phase-space plot that feature at least a probability of occurrence of 10^{-3}, 10^{-4}, 10^{-5}, 10^{-6} are given for the six configurations for which the phase-space plots have been generated: (i) CM measurement, (ii) SI measurement, (iii) CM measurement *vs.* 30 μm ARS measurement, (iv) CM measurement *vs.* 900 μm ARS measurement, (v) SI measurement *vs.* 30 μm ARS measurement, (vi) SI measurement *vs.* 900 μm ARS measurement. The representation follows a similar concept to the Abbott-curve and various numeric parameters can be generated to quantitatively assess and compare the results in the phase-space representation. This approach would also allow to use the representation for process monitoring.

The overall functions of $A(p^*)$ are illustrated in Fig. 19 for the CLs 1–15. The relative area features the dimension $\mu m \bullet^{\circ}$. In this representation, the previous observations can be confirmed on a quantitative level: The applied lightspot diameter does not influence the results of the measured angular distribution, the SI data is much closer to the ARS angular data than the angles determined based on the CM measurement. Additionally, the combination of height measurements of CM and SI with ARS results makes the results significantly more comparable and reproducible. From this, the conclusion can be drawn that a combination of the two perspectives – heights and angles – is meaningful and provides more comprehensive insights than evaluating a phase-space only based on height topography data since in the angular data of numerical differentiation many instrument-specific characteristics are included and enhanced. The ARS sensor allows a reliable and direct characterization of the angular distribution that can give additional insights into the state of the surface. The suggested representation and the associated parameters can serve as an approach for the tribological monitoring or surfaces just as well as manufacturing processes, as they can quantitatively expose changes in the probability distribution shown in the phase-space diagram.

5. Conclusion

The comparability of tactile and optical measurement methods is inherently limited due to the fundamentally different physical principles they rely on. This makes direct data comparison challenging, especially when aiming for functional surface characterization and illustrates that topography height information does depend on the characteristics of the applied measuring principle and instrument. Thus, it was examined to

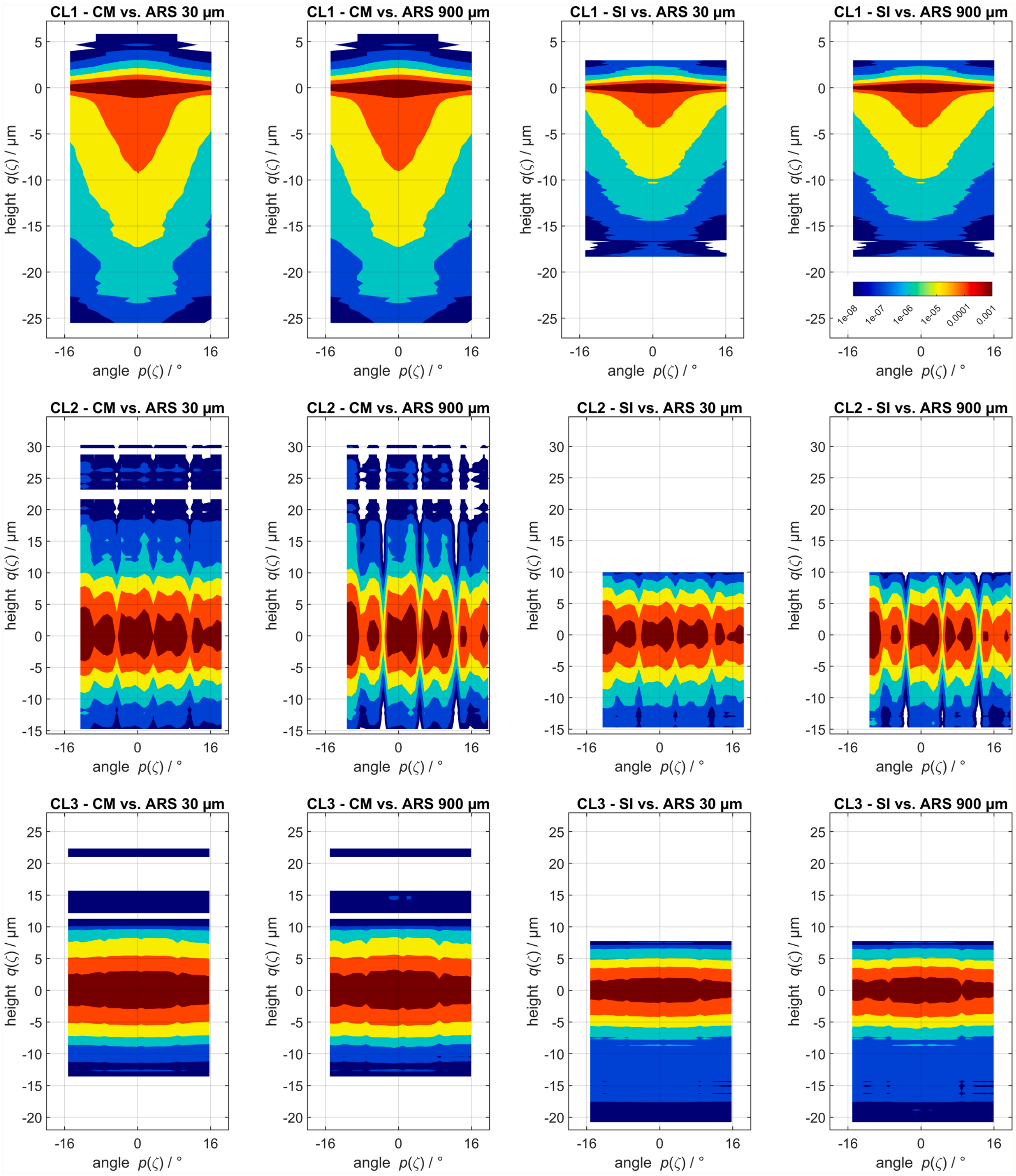

Fig. 18. Phase-space plot of all optical confocal microscope (CM), and tactile stylus instrument (SI) height topography data combined with ARS light measurement featuring 30 μm and 900 μm lightspots. The topography data was processed profile-wise with a linear S-filtering (ISO 16610-21) $N_{is} = 2.5\mu m$, a subtraction of a fitted least squares straight line and L-filtering with a robust Gaussian filter of second order (ISO 16610-31), $N_{iL} = 1.285mm$. The data of cylinder liners 1–3 is summarized.

what extent the fusion of height and angular information of surface topography can provide improved insights into the functionality of workpieces.

To explore this, a case study involving 15 cylinder liners was conducted, examining how each measurement method captures tribologically relevant surface features. Measurements using a stylus instrument, a confocal microscope and an angular-resolved scattering light sensor were considered. In the evaluations, the following observations could be made:

(1) Generally, even though some features are transferred differently and artefacts related to the physics of the measuring principles

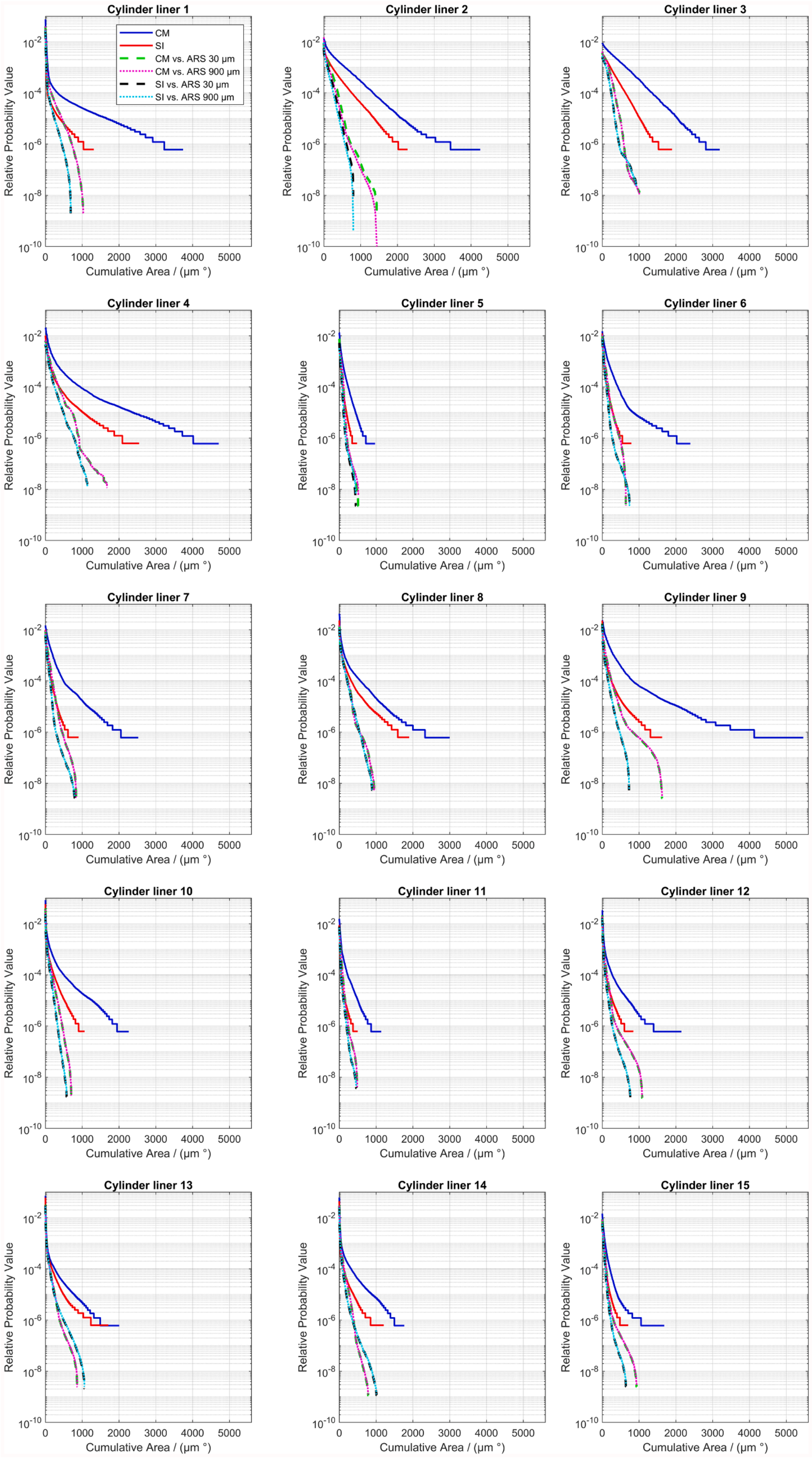

Fig. 19. Relative probability as function of the cumulative area in the phase-space diagram for different measuring principles and their combinations.

occurred, in many cases similar height distributions and resulting from that also similar surface texture parameters could be obtained by both tactile and optical measurement. The reason is that many parameters perform an averaging of the height distribution that can be robust to nonlinear effects, however also results in the loss of information since the lateral scale is neglected. This can in many circumstances reduce the information content available in the height distribution or parameters derived from it since with regard to the functional performance of surfaces minor changes that can influence the tribological performance not necessarily reflect in the height-based parameters.

(2) When the angular distributions and also the angular parameters obtained by the stylus instrument and confocal microscope were compared, more significant differences could be exposed as the derivative is more sensitive with regard to minor changes in the surface topography. Thus, often in functional characterization the surface gradient or associated parameters are used for process monitoring or comparison. When comparing the angular results for the different applied measuring principles including a direct measurement using the ARS sensor, it was shown that mostly, the stylus measurement had a better agreement to the angular distributions measured by the ARS sensor.

(3) These findings suggest that for a meaningful functional evaluation, it is beneficial to consider both the height and angular distribution of surface features. These two perspectives offer complementary insights into how a surface behaves under tribological stress.

(4) To better understand and model tribological processes, the use of a phase-space representation was examined and recommended. This approach allows to visualize and analyze the dynamic interplay between surface geometry and functional behavior in a more integrated and insightful way, also showing smaller deviations between different measurements, that for example many surface texture parameters or a sole monitoring or comparison of the height distribution cannot always expose. This visualization of the probability of different classes in the phase-space demonstrated that minor changes in both the height and angular distribution can be monitored and highlighted.

(5) Due to the challenges in numerical differentiation, it can also be meaningful to combine the height distribution of a surface topography measurement with the angular distribution of an ARS light measurement into a multimodal phase-space representation resulting in a better comparability and reproducibility of the results.

(6) It could be illustrated that the phase-space representation can expose changes in the state of the surface, that are also linked to its tribological characteristics, using quantitative metrics that can for example describe the area in the phase-space where a certain probability value is exceeded. In future work, the quantitative correlation and connection to known tribological performance metrics like friction coefficients will be examined.

The suggested phase-space representation introduces a novel visualization that can represent minor changes in the height and angular distribution in a compact diagram so that they can be detected easily. In cases that only one of the distributions is affected in the context of a tribological process, for example when the functionality changes, but this is not reflected in the height distribution or its associated parameters but only in the angular distribution, the fusion of information that is inherent in this representation allows an efficient determination of a change of state of the surface. The potential of this approach for the monitoring of tribological processes will be explored further in future work.

Author Contributions

Both authors contributed to the study conception and design. ARS measurements were performed by both authors. The data analysis and visualization were performed by Matthias Eifler (M.E.). The first draft of the manuscript was written by M.E. and all authors commented on previous versions of the manuscript. All authors read and approved the final manuscript.

CRediT authorship contribution statement

Matthias Eifler: Writing – review & editing, Writing – original draft, Visualization, Validation, Supervision, Methodology, Investigation, Formal analysis, Data curation, Conceptualization. **Boris Brodmann:** Writing – review & editing, Methodology, Investigation, Conceptualization.

Funding

This research received no external funding.

Declaration of competing interest

The authors declare the following financial interests/personal relationships which may be considered as potential competing interests: Matthias Eifler reports administrative support and article publishing charges were provided by IU University of Applied Sciences. If there are other authors, they declare that they have no known competing financial interests or personal relationships that could have appeared to influence the work reported in this paper.

Acknowledgements

We would like to acknowledge Sebastian Rief for the support of the topography measurement data acquisition.

Appendix A. Profile surface texture parameters

.

Table 1

95 % confidence intervals of profile surface texture parameters. The distributions of all 400 evaluated profiles (optical) and 125 evaluated profiles (tactile) are shown for the cylinder liners 1–15. The amplitude-based parameters R_a, R_q, R_{sk}, R_{ku}, R_t and attribute parameters based on peak heights and pit depths R_z are displayed.

CL No.	$R_a/\mu m$ *CM*	$R_a/\mu m$ *SI*	$R_q/\mu m$ *CM*	$R_q/\mu m$ *SI*	$R_{zn}/\mu m$ *CM*	$R_{zn}/\mu m$ *SI*	R_{sk} *CM*	R_{sk} *SI*	R_{ku} *CM*	R_{ku} *SI*	$R_t/\mu m$ *CM*	$R_t/\mu m$ *SI*
1	0.402	0.386	1.211	1.134	9.119	8.792	−5.816	−5.851	42.017	43.468	13.291	13.084
	± 0.158	± 0.142	± 0.557	± 0.477	± 2.733	± 2.824	± 1.450	± 1.721	± 24.288	± 28.905	± 4.878	± 5.409
2	1.229	1.411	1.657	1.864	10.779	12.236	0.597	−0.010	4.509	4.307	13.903	15.515

(*continued on next page*)

Table 1 (*continued*)

CL No.	R_a/*μm CM*	R_a/*μm SI*	R_q/*μm CM*	R_q/*μm SI*	R_{zn}/*μm CM*	R_{zn}/*μm SI*	R_{sk} *CM*	R_{sk} *SI*	R_{ku} *CM*	R_{ku} *SI*	R_t/*μm CM*	R_t/*μm SI*
	± 0.067	± 0.168	± 0.105	± 0.245	± 1.523	± 2.189	± 0.412	± 0.987	± 2.960	± 1.778	± 5.719	± 4.165
3	1.099	1.222	1.406	1.570	8.968	9.888	0.146	−0.440	3.542	4.567	11.103	12.956
	± 0.078	± 0.150	± 0.104	± 0.233	± 1.004	± 2.050	± 0.375	± 0.957	± 0.669	± 7.468	± 2.307	± 6.534
4	1.020	1.125	1.637	1.791	12.929	13.277	1.527	1.888	10.196	9.554	18.815	18.952
	± 0.231	± 0.182	± 0.372	± 0.333	± 2.758	± 2.530	± 1.130	± 1.068	± 10.539	± 4.706	± 6.086	± 5.836
5	0.397	0.397	0.521	0.522	3.584	3.908	−1.213	−0.971	6.916	6.480	5.202	5.621
	± 0.022	± 0.024	± 0.047	± 0.055	± 0.924	± 0.990	± 1.256	± 1.222	± 19.383	± 14.733	± 3.511	± 3.262
6	0.599	0.623	0.940	0.930	6.540	6.037	−3.058	−2.640	16.574	14.091	9.599	8.914
	± 0.029	± 0.077	± 0.097	± 0.197	± 1.412	± 1.854	± 0.861	± 1.922	± 10.194	± 30.873	± 3.082	± 6.566
7	0.689	0.723	0.979	1.043	6.572	6.678	−2.224	−2.381	10.285	12.046	9.178	9.731
	± 0.032	± 0.065	± 0.101	± 0.198	± 1.133	± 2.126	± 1.194	± 1.731	± 16.634	± 22.627	± 4.127	± 6.491
8	0.841	1.134	1.573	1.867	9.023	10.340	−3.055	−2.767	12.292	10.980	12.242	14.280
	± 0.063	± 0.442	± 0.156	± 0.377	± 2.295	± 3.006	± 0.514	± 0.958	± 5.369	± 7.730	± 4.080	± 6.183
9	0.864	0.843	1.654	1.566	10.406	9.023	−4.147	−3.194	27.967	14.259	17.174	13.018
	± 0.088	± 0.190	± 0.355	± 0.310	± 3.778	± 2.420	± 2.427	± 1.017	± 42.307	± 12.235	± 10.817	± 6.084
10	0.738	0.855	1.308	1.432	7.055	7.670	−2.874	−2.743	10.887	10.136	9.257	10.059
	± 0.028	± 0.244	± 0.070	± 0.237	± 0.928	± 1.365	± 0.313	± 0.668	± 3.165	± 6.000	± 2.094	± 3.173
11	0.293	0.236	0.412	0.451	3.314	4.304	−2.322	−5.058	16.770	47.913	5.259	6.851
	± 0.023	± 0.070	± 0.065	± 0.234	± 0.986	± 1.901	± 1.540	± 4.097	± 21.203	± 88.160	± 2.195	± 5.463
12	0.392	0.408	0.810	0.825	5.349	6.008	−4.144	−4.074	25.615	25.616	8.554	9.286
	± 0.035	± 0.073	± 0.191	± 0.272	± 1.629	± 2.158	± 2.251	± 2.253	± 40.845	± 37.166	± 6.625	± 6.784
13	0.415	0.571	0.899	1.306	6.468	8.623	−3.947	−4.447	22.036	28.802	9.401	14.033
	± 0.040	± 0.183	± 0.156	± 0.551	± 1.607	± 3.249	± 1.411	± 2.176	± 24.174	± 31.150	± 4.544	± 8.728
14	0.468	0.475	0.956	1.019	6.299	7.328	−3.577	−4.166	16.811	26.014	8.675	11.418
	± 0.040	± 0.116	± 0.116	± 0.381	± 1.117	± 3.238	± 0.670	± 1.993	± 9.913	± 30.131	± 3.318	± 7.881
15	0.382	0.436	0.569	0.647	4.556	5.158	−3.197	−2.818	31.995	20.703	8.295	8.139
	± 0.019	± 0.038	± 0.135	± 0.148	± 1.797	± 1.673	± 4.274	± 2.952	± 86.722	± 51.046	± 7.101	± 5.879

Table 2

95 % confidence intervals of profile surface texture parameters. The distributions of all 400 evaluated profiles (optical) and 125 evaluated profiles (tactile) are shown for the cylinder liners 1–15. The hybrid parameters R_{dq}, R_{dt}, R_{dl}, R_{da} are displayed.

CL No.	R_{dq} *CM*	R_{dq} *SI*	R_{dt} *CM*	R_{dt} *SI*	R_{dl}/*μm CM*	R_{dl}/*μm SI*	R_{da} *CM*	R_{da} *SI*
1	0.165	0.076	2.487	1.291	12,592	12,568	0.091	0.029
	± 0.050	± 0.015	± 1.254	± 0.422	± 48	± 26	± 0.014	± 0.004
2	0.284	0.179	1.615	1.335	12,804	12,880	0.260	0.096
	± 0.013	± 0.016	± 1.104	± 0.297	± 21	± 65	± 0.009	± 0.009
3	0.323	0.184	1.456	1.229	12,894	12,902	0.307	0.101
	± 0.010	± 0.013	± 0.594	± 0.274	± 22	± 55	± 0.009	± 0.007
4	0.201	0.112	2.097	1.340	12,649	12,649	0.161	0.054
	± 0.025	± 0.009	± 1.387	± 0.300	± 32	± 22	± 0.014	± 0.004
5	0.120	0.072	0.727	0.678	12,557	12,564	0.106	0.037
	± 0.009	± 0.004	± 0.518	± 0.333	± 8	± 7	± 0.008	± 0.002
6	0.144	0.076	1.519	0.977	12,580	12,570	0.119	0.036
	± 0.014	± 0.007	± 0.995	± 0.530	± 12	± 11	± 0.005	± 0.002
7	0.157	0.085	1.565	1.017	12,593	12,588	0.130	0.042
	± 0.015	± 0.008	± 1.086	± 0.470	± 13	± 15	± 0.007	± 0.003
8	0.181	0.114	1.967	1.383	12,620	12,656	0.128	0.052
	± 0.024	± 0.024	± 1.149	± 0.337	± 25	± 64	± 0.009	± 0.013
9	0.219	0.100	3.086	1.283	12,661	12,620	0.160	0.045
	± 0.060	± 0.012	± 2.538	± 0.333	± 57	± 26	± 0.013	± 0.006
10	0.165	0.101	1.413	1.124	12,602	12,623	0.118	0.045
	± 0.009	± 0.016	± 0.605	± 0.340	± 10	± 37	± 0.004	± 0.010
11	0.100	0.058	0.806	0.823	12,539	12,542	0.087	0.029
	± 0.007	± 0.011	± 0.494	± 0.498	± 5	± 15	± 0.005	± 0.004
12	0.125	0.072	1.486	1.066	12,558	12,564	0.091	0.033
	± 0.047	± 0.010	± 1.881	± 0.425	± 31	± 16	± 0.009	± 0.003
13	0.141	0.095	1.530	1.290	12,574	12,607	0.092	0.038
	± 0.020	± 0.015	± 1.143	± 0.427	± 16	± 32	± 0.005	± 0.007
14	0.141	0.080	1.317	1.200	12,575	12,577	0.092	0.031
	± 0.011	± 0.014	± 0.665	± 0.513	± 10	± 26	± 0.006	± 0.004
15	0.116	0.071	1.390	0.951	12,551	12,561	0.098	0.036
	± 0.023	± 0.006	± 1.591	± 0.520	± 14	± 10	± 0.007	± 0.002

Table 3

95 % confidence intervals of profile surface texture parameters. The distributions of all 400 evaluated profiles (optical) and 125 evaluated profiles (tactile) are shown for the cylinder liners 1–15. The parameters based on profile elements: R_{sm} *count* (no. of profile elements), R_{sm}, R_{c}, R_{cmax}, and the attribute parameters R_{pmax}, R_{vmax} are displayed.

CL No.	R_{sm} *count CM*	R_{sm} *count SI*	$R_{\mathrm{sm}}/\mu m$ *CM*	$R_{\mathrm{sm}}/\mu m$ *SI*	$R_{\mathrm{c}}/\mu m$ *CM*	$R_{\mathrm{c}}/\mu m$ *SI*	$R_{\mathrm{cmax}}/\mu m$ *CM*	$R_{\mathrm{cmax}}/\mu m$ *SI*	$R_{\mathrm{pmax}}/\mu m$ *CM*	$R_{\mathrm{pmax}}/\mu m$ *SI*	$R_{\mathrm{vmax}}/\mu m$ *CM*	$R_{\mathrm{vmax}}/\mu m$ *SI*
1	38.35	44.90	0.311	0.267	4.111	3.649	12.627	12.242	1.177	1.333	−12.103	−11.731
	± 10.68	± 12.79	± 0.088	± 0.076	± 1.496	± 1.245	± 4.771	± 5.398	± 0.617	± 0.911	± 4.798	± 5.410
2	155.43	167.38	0.079	0.074	4.319	4.749	10.945	12.378	7.741	7.289	−6.163	−8.225
	± 18.10	± 22.94	± 0.009	± 0.010	± 0.306	± 0.716	± 4.150	± 3.934	± 4.367	± 2.540	± 2.404	± 3.945
3	231.26	216.71	0.053	0.057	3.477	3.878	8.879	10.407	5.768	5.332	−5.334	−7.608
	± 28.30	± 28.10	± 0.007	± 0.007	± 0.248	± 0.523	± 2.065	± 6.042	± 1.859	± 1.769	± 1.422	± 6.124
4	75.97	79.44	0.157	0.151	4.590	4.650	13.952	14.110	10.164	10.470	−8.652	−8.334
	± 15.16	± 17.18	± 0.033	± 0.033	± 0.986	± 0.814	± 5.747	± 5.056	± 5.673	± 3.687	± 2.645	± 4.644
5	215.71	232.74	0.057	0.053	1.389	1.420	4.215	4.354	1.777	2.337	−3.425	−3.284
	± 24.49	± 29.07	± 0.007	± 0.007	± 0.135	± 0.135	± 3.429	± 2.885	± 0.859	± 1.804	± 3.421	± 2.641
6	109.38	129.80	0.111	0.095	2.320	2.260	8.882	8.223	1.396	1.318	−8.197	−7.539
	± 13.43	± 22.58	± 0.014	± 0.017	± 0.234	± 0.360	± 3.116	± 6.498	± 0.289	± 0.277	± 2.927	± 6.486
7	126.62	137.02	0.097	0.090	2.448	2.515	8.215	8.965	1.689	1.649	−7.489	−8.079
	± 15.99	± 23.54	± 0.013	± 0.017	± 0.217	± 0.422	± 3.957	± 6.464	± 0.306	± 0.868	± 4.091	± 6.552
8	93.91	105.85	0.130	0.117	3.284	3.950	11.640	13.611	1.043	1.324	−11.199	−12.925
	± 13.08	± 19.50	± 0.019	± 0.022	± 0.493	± 1.035	± 4.021	± 6.017	± 0.623	± 1.332	± 4.018	± 5.844
9	96.58	102.03	0.128	0.121	3.451	3.282	16.600	12.382	1.259	0.988	−15.913	−11.937
	± 24.41	± 22.66	± 0.032	± 0.029	± 0.853	± 0.588	± 10.840	± 5.906	± 0.669	± 0.901	± 10.722	± 5.841
10	115.25	135.89	0.107	0.092	2.641	2.845	9.017	9.745	0.499	0.638	−8.758	−9.404
	± 12.45	± 29.02	± 0.011	± 0.020	± 0.215	± 0.417	± 2.108	± 3.036	± 0.258	± 0.823	± 2.107	± 2.989
11	147.80	173.90	0.084	0.078	1.058	1.159	4.479	6.084	1.294	1.172	−3.965	−5.674
	± 39.23	± 109.59	± 0.027	± 0.062	± 0.207	± 0.613	± 2.113	± 5.388	± 0.383	± 0.898	± 2.130	± 5.364
12	98.06	114.02	0.125	0.108	1.934	2.033	8.047	8.604	0.859	1.068	−7.677	−8.218
	± 20.75	± 30.67	± 0.026	± 0.030	± 0.380	± 0.529	± 6.544	± 6.746	± 0.456	± 1.335	± 6.518	± 6.727
13	79.21	86.50	0.151	0.141	2.485	3.056	8.540	12.992	1.137	1.288	−8.244	−12.690
	± 13.98	± 25.10	± 0.027	± 0.041	± 0.394	± 0.756	± 4.688	± 8.859	± 1.223	± 1.781	± 4.695	± 8.828
14	70.18	67.84	0.172	0.178	2.689	2.930	7.876	10.403	1.083	1.213	−7.510	−10.005
	± 9.21	± 13.36	± 0.023	± 0.036	± 0.302	± 0.755	± 3.189	± 7.449	± 0.853	± 1.761	± 3.241	± 7.371
15	159.81	162.42	0.078	0.077	1.452	1.658	7.314	7.223	1.625	1.591	−6.666	−6.545
	± 43.44	± 42.89	± 0.023	± 0.023	± 0.298	± 0.314	± 6.986	± 5.874	± 1.197	± 0.559	± 7.027	± 5.865

Table 4

95 % confidence intervals of profile surface texture parameters. The distributions of all 400 evaluated profiles (optical) and 125 evaluated profiles (tactile) are shown for the cylinder liners 1–15. The parameters for stratified surfaces using the material ratio curve: R_{k}, R_{pk}, R_{vk} are displayed.

CL No.	$R_{\mathrm{k}}/\mu m$ *CM*	$R_{\mathrm{k}}/\mu m$ *SI*	$R_{\mathrm{pk}}/\mu m$ *CM*	$R_{\mathrm{pk}}/\mu m$ *SI*	$R_{\mathrm{vk}}/\mu m$ *CM*	$R_{\mathrm{vk}}/\mu m$ *SI*
1	0.465	0.452	0.251	0.265	3.292	2.978
	± 0.034	± 0.062	± 0.057	± 0.100	± 1.721	± 1.300
2	3.095	3.820	2.329	2.165	1.825	2.399
	± 0.275	± 0.652	± 0.309	± 0.396	± 0.296	± 0.809
3	3.419	3.822	1.551	1.432	1.426	1.834
	± 0.293	± 0.494	± 0.310	± 0.441	± 0.170	± 0.508
4	1.937	2.204	3.086	3.438	2.229	1.988
	± 0.290	± 0.348	± 0.847	± 0.833	± 0.529	± 0.704
5	1.192	1.193	0.354	0.411	0.724	0.707
	± 0.097	± 0.081	± 0.068	± 0.101	± 0.085	± 0.130
6	1.476	1.557	0.341	0.300	1.807	1.705
	± 0.124	± 0.192	± 0.084	± 0.093	± 0.211	± 0.405
7	1.850	1.913	0.367	0.349	1.662	1.815
	± 0.150	± 0.179	± 0.098	± 0.096	± 0.204	± 0.439
8	0.838	1.544	0.193	0.218	3.235	3.555
	± 0.072	± 1.619	± 0.068	± 0.200	± 0.266	± 0.557
9	1.155	0.835	0.235	0.162	3.088	3.132
	± 0.087	± 0.242	± 0.047	± 0.104	± 0.445	± 0.440
10	0.692	0.860	0.073	0.082	2.528	2.756
	± 0.083	± 0.537	± 0.022	± 0.098	± 0.130	± 0.399
11	0.860	0.542	0.270	0.204	0.613	0.906
	± 0.064	± 0.061	± 0.057	± 0.051	± 0.146	± 0.541
12	0.588	0.598	0.179	0.182	1.830	1.780
	± 0.047	± 0.068	± 0.062	± 0.075	± 0.235	± 0.413
13	0.463	0.480	0.191	0.221	2.083	2.643
	± 0.030	± 0.099	± 0.094	± 0.183	± 0.257	± 0.747
14	0.598	0.536	0.218	0.215	2.207	2.145
	± 0.047	± 0.077	± 0.129	± 0.237	± 0.242	± 0.580
15	1.046	1.182	0.311	0.331	0.946	1.120
	± 0.060	± 0.096	± 0.069	± 0.065	± 0.184	± 0.276

Table 5

95 % confidence intervals of profile surface texture parameters. The distributions of all 400 evaluated profiles (optical) and 125 evaluated profiles (tactile) are shown for the cylinder liners 1–15. The attribute parameters based on peak heights and pit depths R_{p}, R_{v} are displayed.

CL No.	$R_{\mathrm{p}}/\mu m$ *CM*	$R_{\mathrm{p}}/\mu m$ *SI*	$R_{\mathrm{v}}/\mu m$ *CM*	$R_{\mathrm{v}}/\mu m$ *SI*
1	0.824	0.896	8.299	7.911
	± 0.239	± 0.359	± 2.708	± 2.816
2	5.986	5.875	4.793	6.378
	± 1.212	± 1.211	± 0.724	± 1.990
3	4.681	4.380	4.287	5.516
	± 0.956	± 1.004	± 0.560	± 1.609
4	7.237	7.783	5.693	5.524
	± 1.870	± 1.939	± 1.578	± 1.822
5	1.360	1.631	2.226	2.277
	± 0.333	± 0.472	± 0.847	± 0.809
6	1.200	1.130	5.375	4.908
	± 0.170	± 0.144	v1.312	v1.842
7	1.442	1.395	5.140	5.285
	± 0.166	± 0.221	± 1.104	± 2.133
8	0.745	1.061	8.284	9.286
	± 0.189	± 0.967	± 2.265	± 2.662
9	0.999	0.714	9.407	8.319
	± 0.216	± 0.356	± 3.786	± 2.356
10	0.406	0.494	6.650	7.188
	± 0.077	± 0.384	± 0.936	± 1.241
11	1.044	0.826	2.276	3.484
	± 0.180	± 0.267	± 0.915	± 1.873
12	0.665	0.713	4.684	5.303
	± 0.233	± 0.323	± 1.542	± 2.147
13	0.655	0.690	5.817	7.949
	± 0.335	± 0.466	± 1.661	± 3.310
14	0.684	0.699	5.615	6.641
	± 0.265	± 0.438	± 1.124	± 3.128
15	1.185	1.274	3.375	3.889
	± 0.316	± 0.240	± 1.732	± 1.679

Table 6

95 % confidence intervals of angular ARS light parameters. The distributions of all 62,500 evaluation positions per cylinder liner are shown for the 900 μm lightspot and 30 μm lightspot each. The statistical moments variance, skewness and kurtosis of the angular distribution A_{q}, A_{sk}, A_{ku} are shown.

CL No.	$A_{\mathrm{q}} - 30\ \mu m$	$A_{\mathrm{q}} - 900\ \mu m$	$A_{\mathrm{sk}} - 30\ \mu m$	$A_{\mathrm{sk}} - 900\ \mu m$	$A_{\mathrm{ku}} - 30\ \mu m$	$A_{\mathrm{ku}} - 900\ \mu m$
1	33.733	35.532	0.072	0.055	3.734	3.263
	± 22.523	± 3.111	± 0.778	± 0.081	± 2.107	± 0.186
2	86.518	77.468	0.200	0.139	2.500	2.174
	± 71.004	± 57.268	± 1.392	± 1.050	± 2.713	± 1.627
3	86.702	83.711	0.014	0.020	2.007	2.062
	± 16.378	± 5.387	± 0.310	± 0.079	± 0.328	± 0.085
4	95.636	97.482	−0.028	0.023	1.862	1.864
	± 10.181	± 4.193	± 0.191	± 0.061	± 0.163	± 0.051
5	36.881	79.390	0.032	−0.407	3.309	2.160
	± 16.861	± 18.261	± 0.552	± 0.307	± 1.208	± 0.448
6	34.300	35.173	0.077	0.021	3.574	3.332
	± 18.007	± 2.524	± 0.599	± 0.065	± 1.433	± 0.159
7	40.301	40.886	0.101	0.046	3.101	3.003
	± 15.511	± 4.195	± 0.471	± 0.092	± 0.906	± 0.196
8	56.250	56.618	−0.070	−0.079	2.607	2.502
	± 20.307	± 7.090	± 0.572	± 0.165	± 0.886	± 0.209
9	43.971	47.012	0.249	0.224	3.145	2.867
	± 20.339	± 10.362	± 0.481	± 0.185	± 1.218	± 0.498
10	32.929	31.078	0.283	0.171	4.518	4.056
	± 29.031	± 7.083	± 0.635	± 0.076	± 4.284	± 0.705
11	49.913	54.542	0.284	0.235	2.834	2.581
	± 15.846	± 12.053	± 0.358	± 0.175	± 0.719	± 0.393
12	35.073	36.729	0.259	0.209	3.453	3.249
	± 8.802	± 4.642	± 0.259	± 0.106	± 0.654	± 0.276
13	38.963	41.028	0.131	0.068	3.326	3.065
	± 22.050	± 9.574	± 0.513	± 0.093	± 1.461	± 0.443
14	28.288	29.428	0.231	0.140	3.823	3.645
	± 11.451	± 4.796	± 0.295	± 0.098	± 0.950	± 0.339
15	42.540	45.548	0.249	0.167	3.196	2.845
	± 22.422	± 5.853	± 0.632	± 0.108	± 1.532	± 0.252

Appendix B. Additional angular distributions

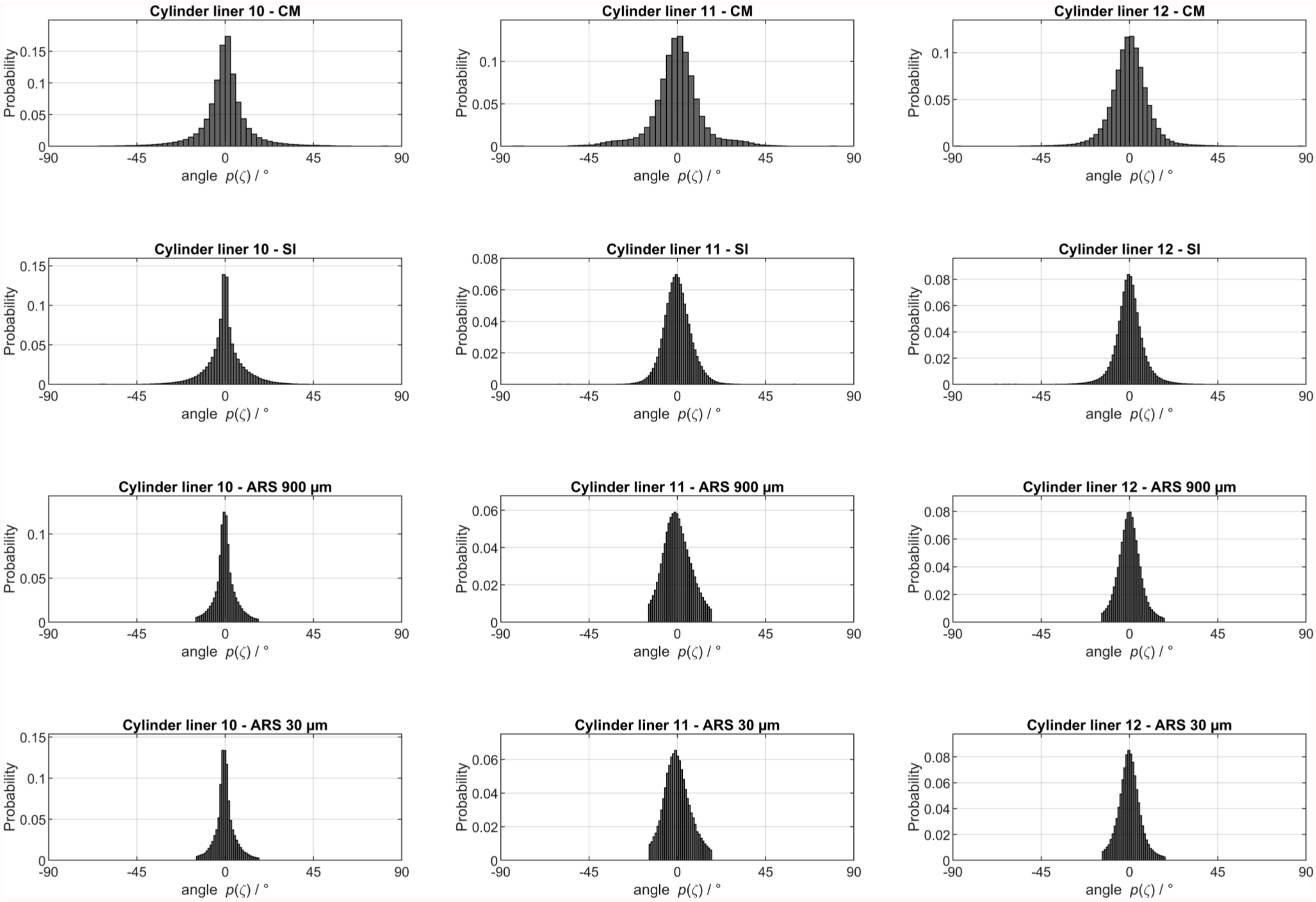

Fig. 20. Angular distributions of all optical confocal microscope (CM), and tactile stylus instrument (SI) height topography data. The topography data was processed profile-wise with a linear S-filtering (ISO 16610-21) $N_{is} = 2.5\mu m$, a subtraction of a fitted least squares straight line and L-filtering with a robust Gaussian filter of second order (ISO 16610-31), $N_{iL} = 1.285mm$. Additionally, the directly measured angular distributions using the ARS light sensor featuring lightspot diameters of 900 µm and 30 µm are shown. The data of cylinder liners 10-12 is summarized.

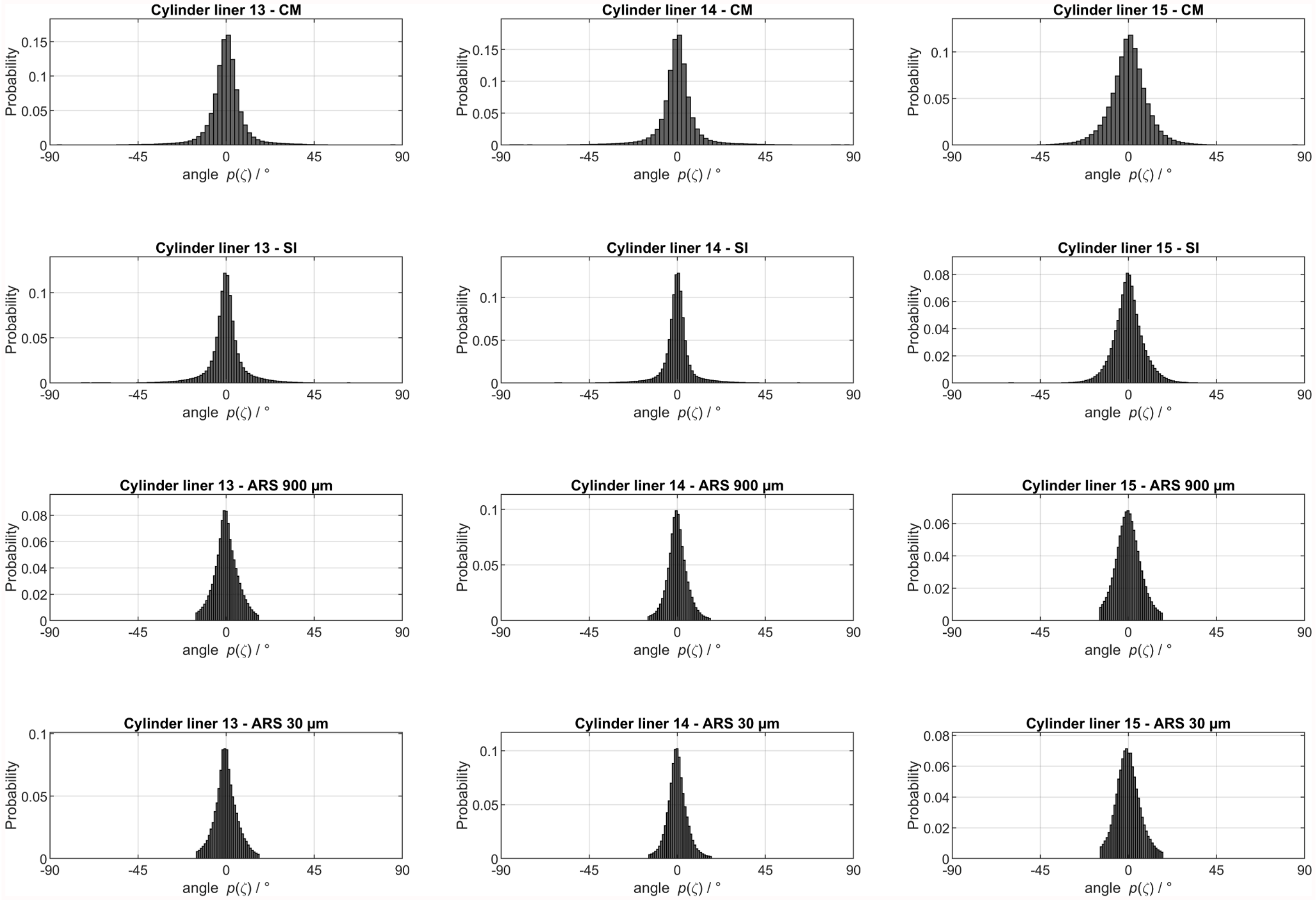

Fig. 21. Angular distributions of all optical confocal microscope (CM), and tactile stylus instrument (SI) height topography data. The topography data was processed profile-wise with a linear S-filtering (ISO 16610–21) $N_{is} = 2.5\mu m$, a subtraction of a fitted least squares straight line and L-filtering with a robust Gaussian filter of second order (ISO 16610–31), $N_{iL} = 1.285mm$. Additionally, the directly measured angular distributions using the ARS light sensor featuring lightspot diameters of 900 μm and 30 μm are shown. The data of cylinder liners 13-15 is summarized.

Appendix C. Additional phase-space representations

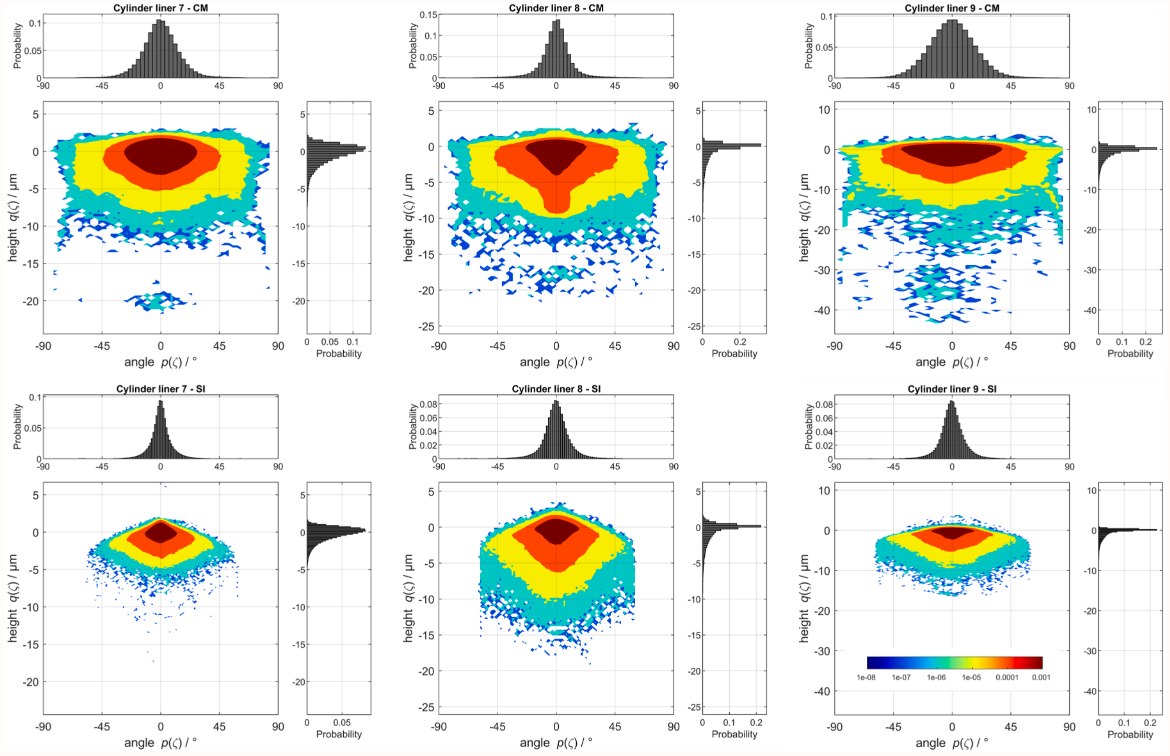

Fig. 22. Phase-space plot of all optical confocal microscope (CM), and tactile stylus instrument (SI) height topography data. The topography data was processed profile-wise with a linear S-filtering (ISO 16610-21) $N_{is} = 2.5\mu m$, a subtraction of a fitted least squares straight line and L-filtering with a robust Gaussian filter of second order (ISO 16610-31), $N_{iL} = 1.285mm$. The data of cylinder liners 7-9 is summarized.

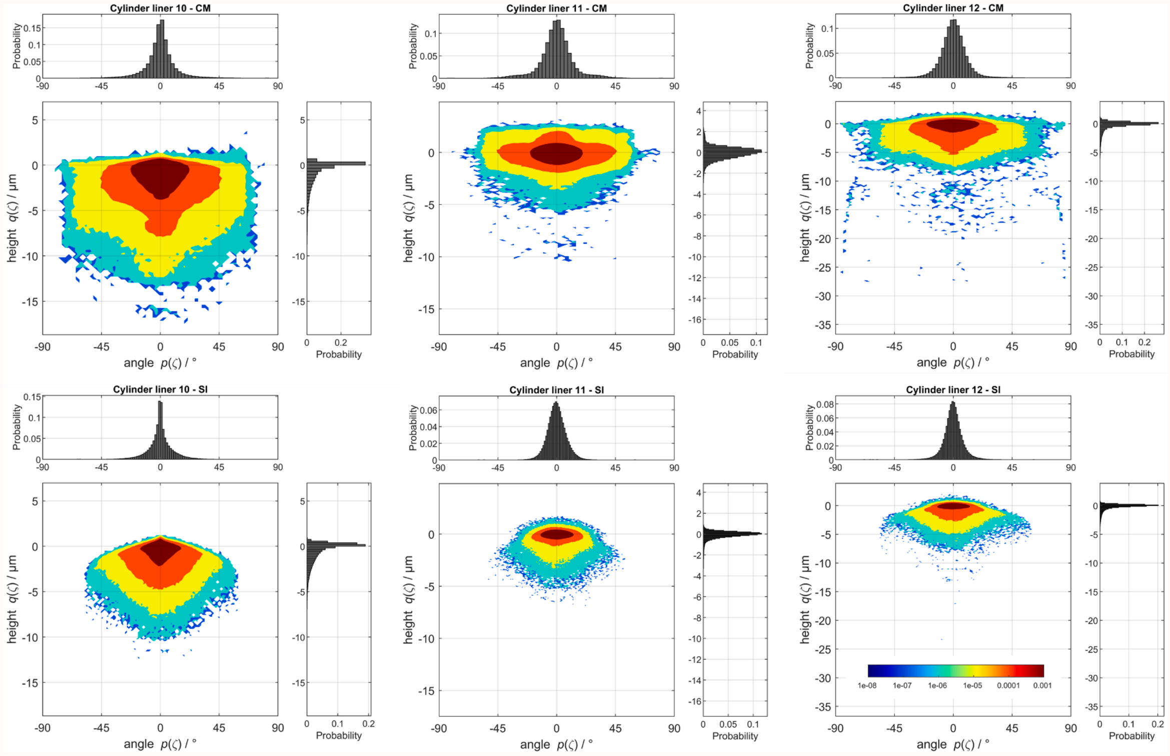

Fig. 23. Phase-space plot of all optical confocal microscope (CM), and tactile stylus instrument (SI) height topography data. The topography data was processed profile-wise with a linear S-filtering (ISO 16610-21) $N_{is} = 2.5\mu m$, a subtraction of a fitted least squares straight line and L-filtering with a robust Gaussian filter of second order (ISO 16610-31), $N_{iL} = 1.285mm$. The data of cylinder liners 10-12 is summarized.

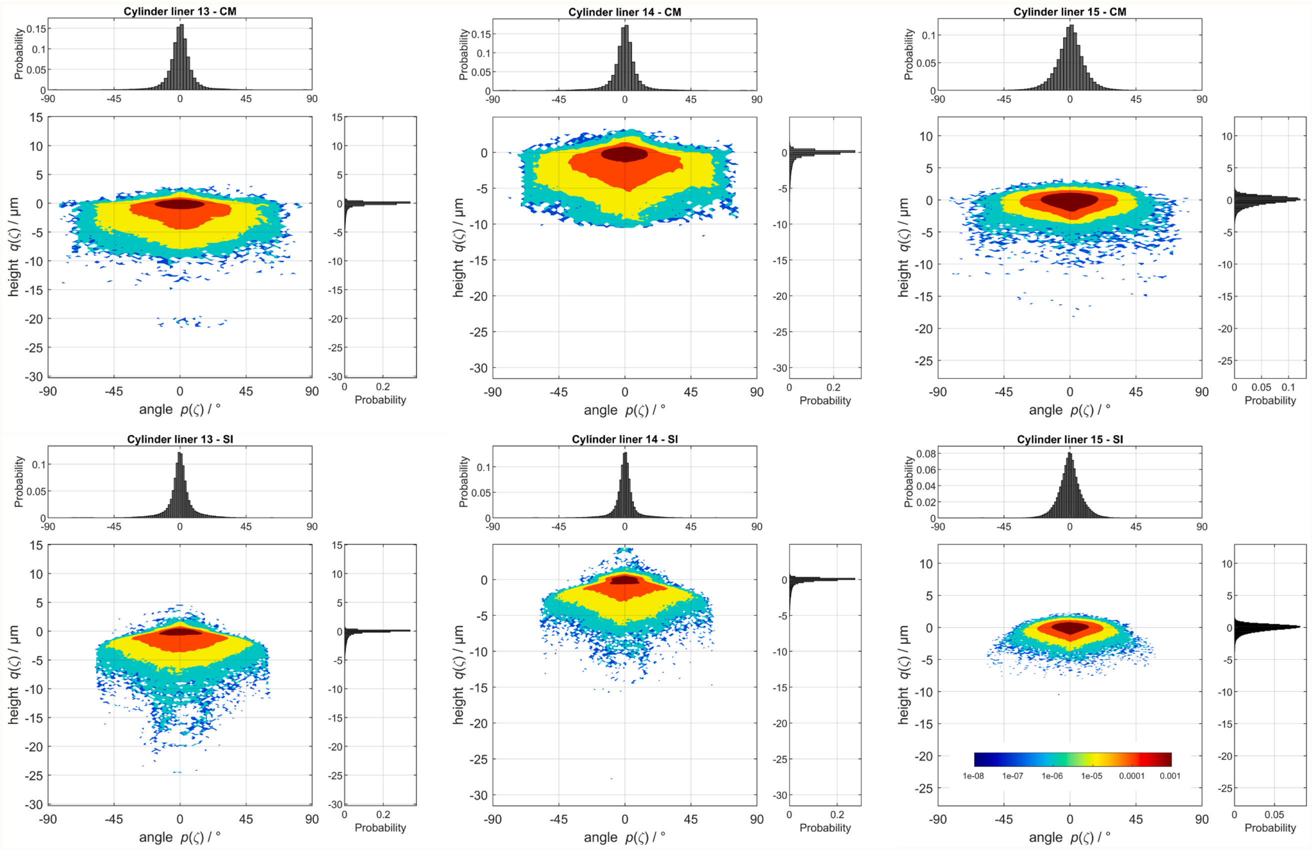

Fig. 24. Phase-space plot of all optical confocal microscope (CM), and tactile stylus instrument (SI) height topography data. The topography data was processed profile-wise with a linear S-filtering (ISO 16610-21) $N_{is} = 2.5\mu m$, a subtraction of a fitted least squares straight line and L-filtering with a robust Gaussian filter of second order (ISO 16610-31), $N_{iL} = 1.285mm$. The data of cylinder liners 13-15 is summarized.

Appendix D. Additional phase-space representations under consideration of ARS measurements

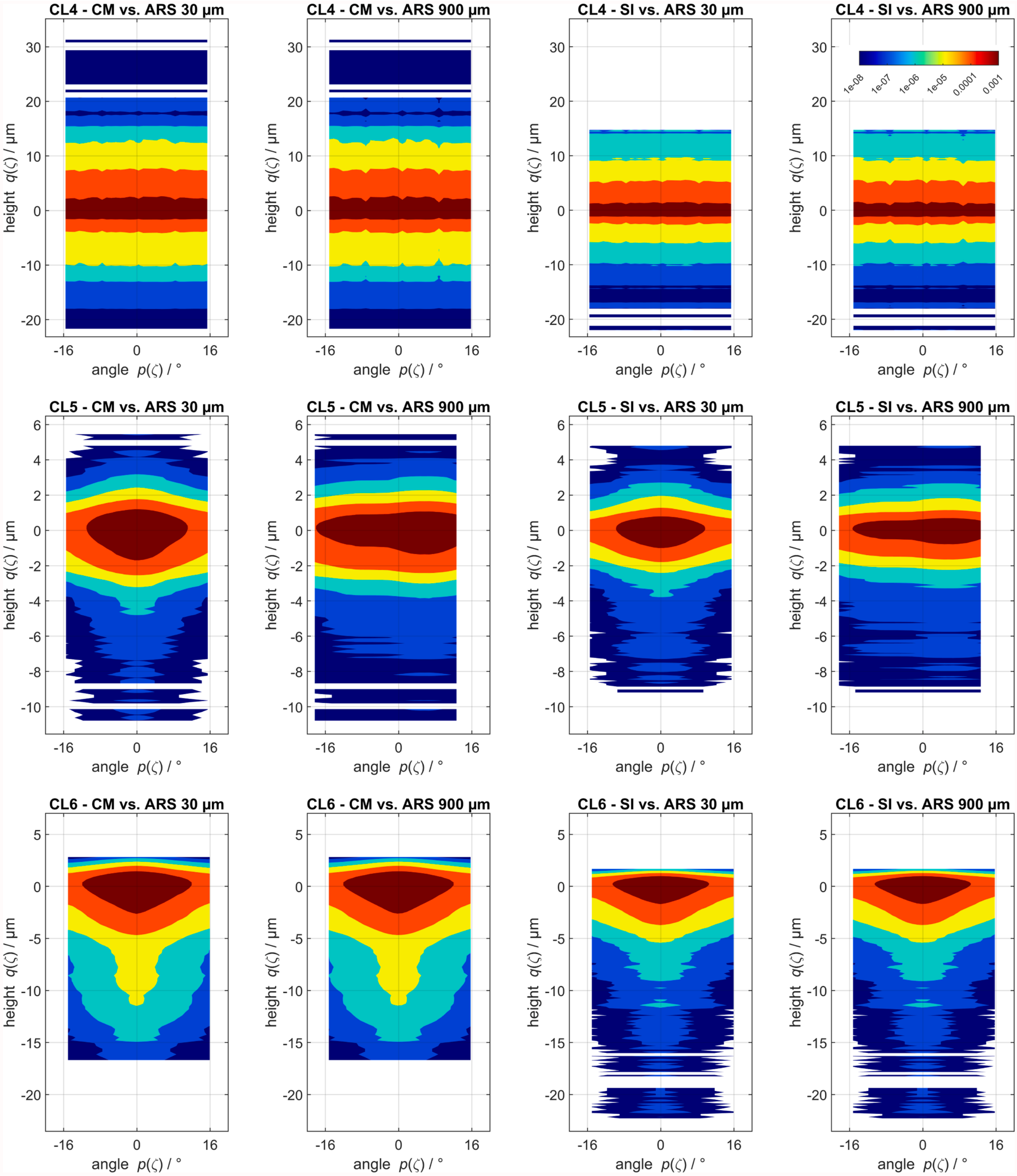

Fig. 25. Phase-space plot of all optical confocal microscope (CM), and tactile stylus instrument (SI) height topography data combined with ARS light measurement featuring 30 µm and 900 µm lightspots. The topography data was processed profile-wise with a linear S-filtering (ISO 16610-21) , a subtraction of a fitted least squares straight line and L-filtering with a robust Gaussian filter of second order (ISO 16610-31), . The data of cylinder liners 4-6 is summarized.

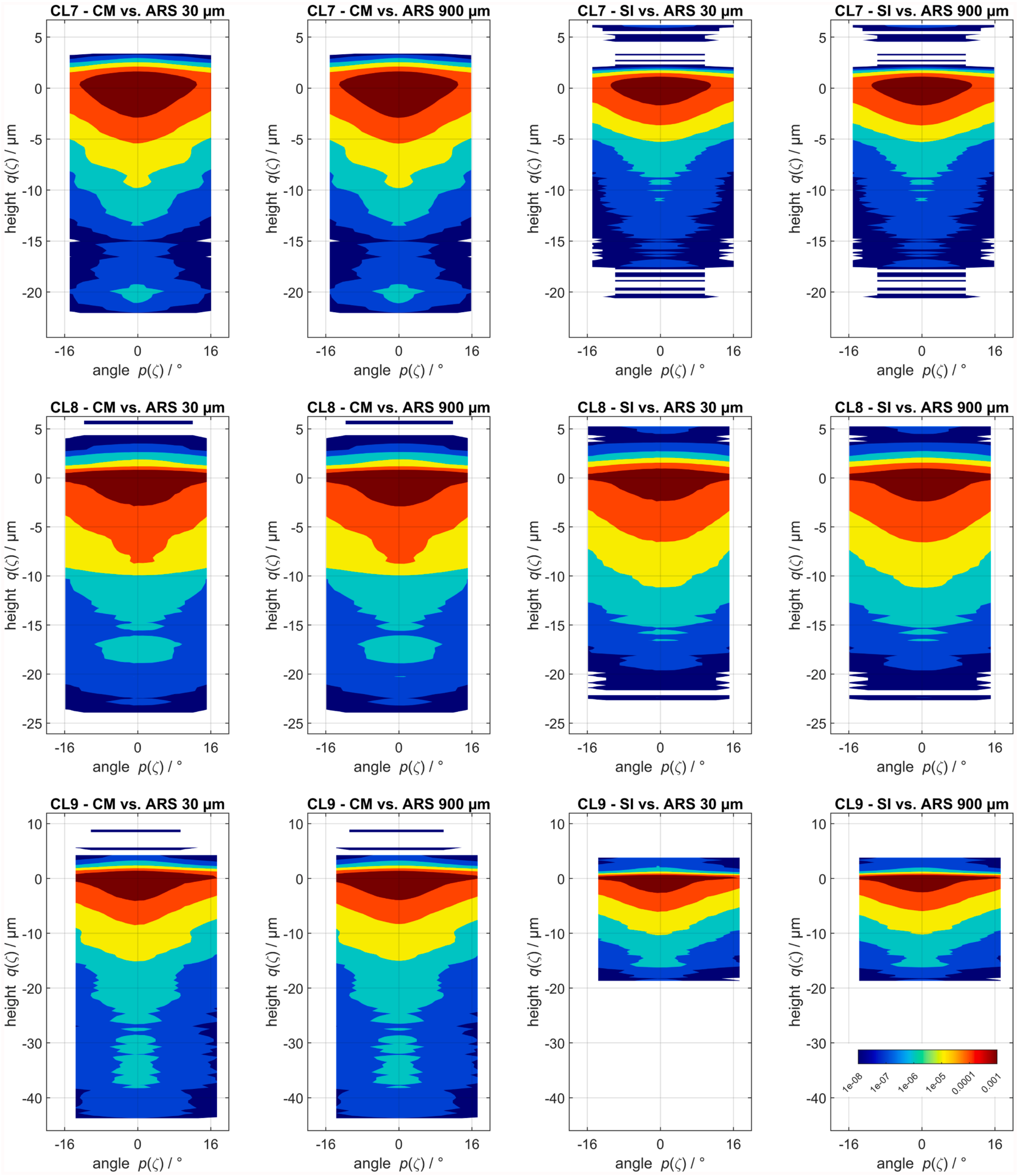

Fig. 26. Phase-space plot of all optical confocal microscope (CM), and tactile stylus instrument (SI) height topography data combined with ARS light measurement featuring 30 µm and 900 µm lightspots. The topography data was processed profile-wise with a linear S-filtering (ISO 16610-21) , a subtraction of a fitted least squares straight line and L-filtering with a robust Gaussian filter of second order (ISO 16610-31), . The data of cylinder liners 7-9 is summarized.

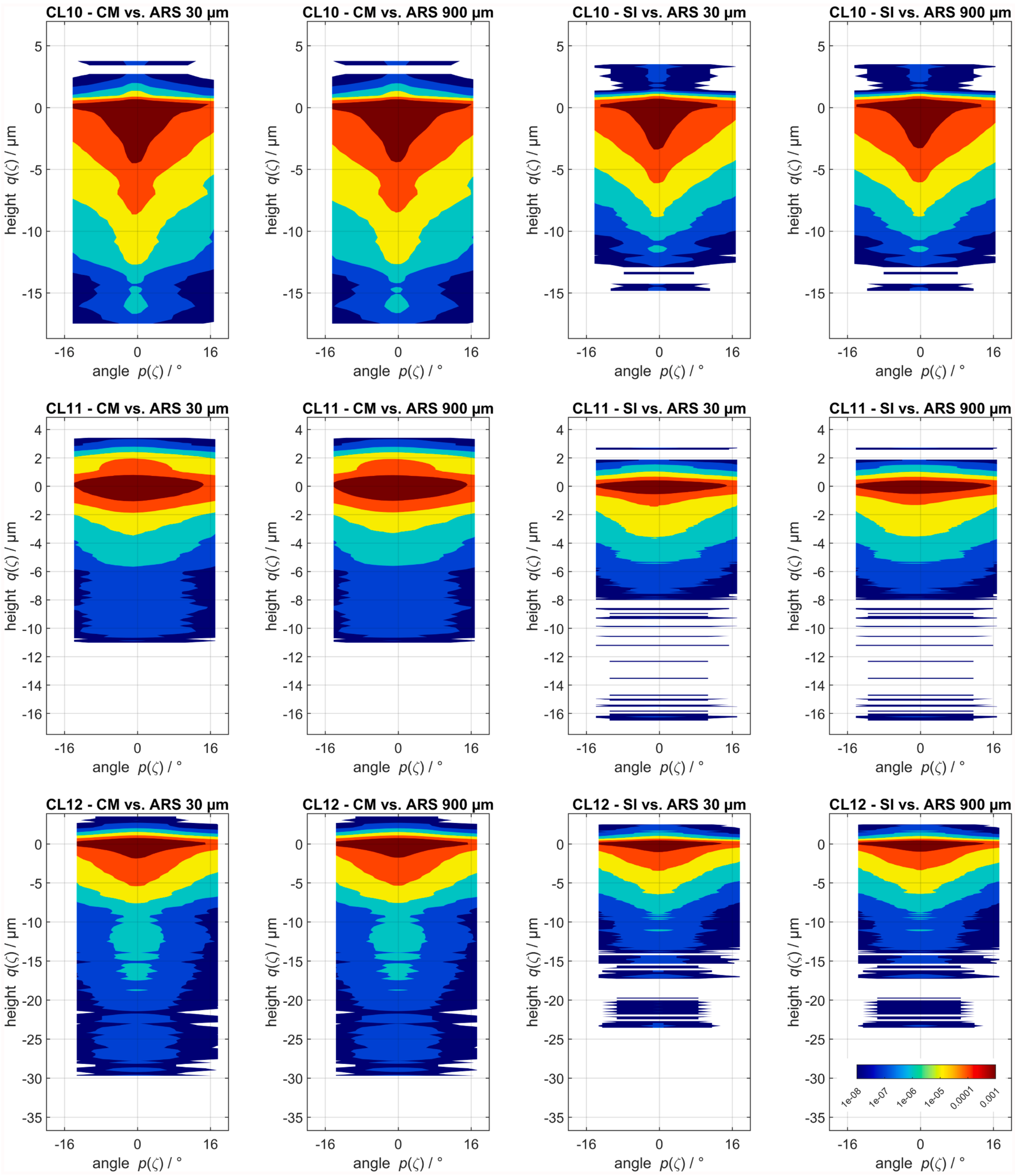

Fig. 27. Phase-space plot of all optical confocal microscope (CM), and tactile stylus instrument (SI) height topography data combined with ARS light measurement featuring 30 µm and 900 µm lightspots. The topography data was processed profile-wise with a linear S-filtering (ISO 16610-21) , a subtraction of a fitted least squares straight line and L-filtering with a robust Gaussian filter of second order (ISO 16610-31), . The data of cylinder liners 10-12 is summarized.

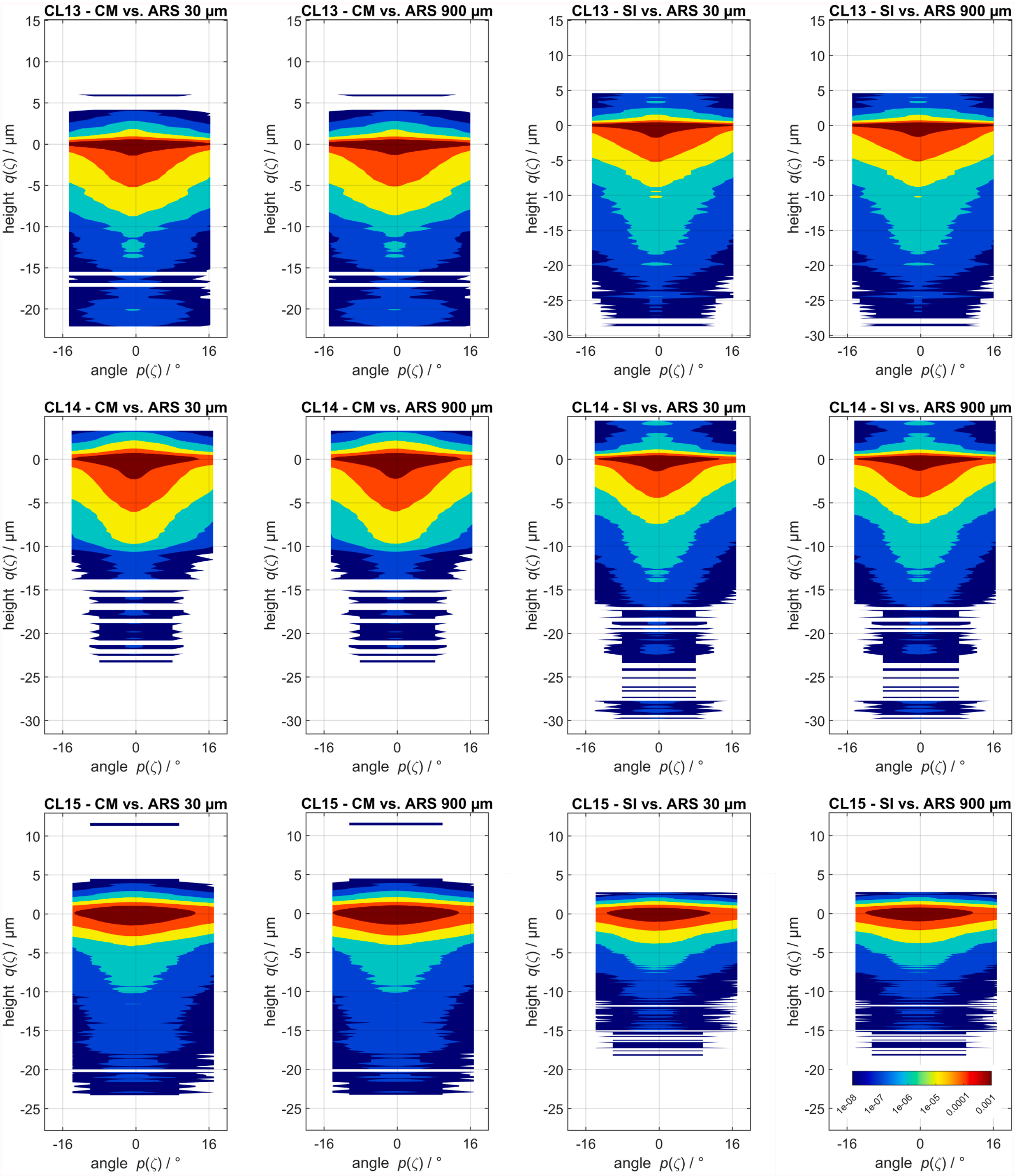

Fig. 28. Phase-space plot of all optical confocal microscope (CM), and tactile stylus instrument (SI) height topography data combined with ARS light measurement featuring 30 µm and 900 µm lightspots. The topography data was processed profile-wise with a linear S-filtering (ISO 16610-21) , a subtraction of a fitted least squares straight line and L-filtering with a robust Gaussian filter of second order (ISO 16610-31), . The data of cylinder liners 13-15 is summarized.

Appendix E. Quantitative comparisons of phase-space representations

Table 7

Cumulative areas in the phase-space featuring a relative probability larger than 10^{-3} and 10^{-4} for the different types of phase-space plots – CM confocal measurement – SI stylus instrument – CM *vs.* ARS 30 µm, CM *vs.* ARS 900 µm – height distribution of CM combined with ARS angular measurement, SI *vs.* ARS 30 µm, SI *vs.* ARS 900 µm – height distribution of SI combined with ARS angular measurement.

CL No.	$A(p^*=10^{-3})$						$A(p^*=10^{-4})$					
	CM	*SI*	*CM vs. ARS 30 µm*	*CM vs. ARS 900 µm*	*SI vs. ARS 30 µm*	*SI vs. ARS 900 µm*	*CM*	*SI*	*CM vs. ARS 30 µm*	*CM vs. ARS 900 µm*	*SI vs. ARS 30 µm*	*SI vs. ARS 900 µm*
1	65.2	17.3	41.5	42.3	23.0	22.8	332.6	58.0	158.7	159.5	77.4	77.7
2	577.6	230.0	163.4	133.0	104.6	85.5	1338.1	759.0	382.4	330.8	296.5	256.5
3	647.1	223.1	171.2	169.4	107.5	104.6	1359.2	630.6	335.3	336.6	241.6	242.8
4	270.6	94.1	127.6	128.1	78.2	78.5	948.0	374.7	367.4	365.0	249.6	249.1
5	87.8	27.1	44.5	57.6	25.5	32.5	241.0	95.2	111.9	120.5	74.6	81.0
6	159.7	32.7	62.9	62.3	36.9	36.9	424.3	127.4	160.1	160.9	112.9	113.1
7	201.0	43.3	80.0	79.1	43.0	42.9	489.1	159.2	189.4	190.0	127.4	127.4
8	139.9	75.9	76.8	77.2	63.7	64.0	572.8	323.5	234.1	234.8	213.7	213.5
9	314.8	57.5	97.9	101.6	51.1	51.7	825.5	247.3	247.9	250.3	160.1	163.2
10	133.1	51.7	61.3	64.1	41.1	42.6	497.9	232.6	182.5	187.0	137.5	141.3
11	63.2	18.0	38.3	39.6	19.6	20.3	227.4	50.8	92.3	94.1	48.3	48.6
12	65.0	20.8	41.1	41.6	23.0	23.3	273.1	99.3	128.3	129.8	78.6	79.7
13	41.9	24.7	33.4	33.9	30.1	30.3	251.5	178.7	117.3	119.9	115.6	118.6
14	50.3	18.6	38.4	39.2	24.0	24.1	321.3	114.5	130.3	132.3	87.7	89.2
15	79.5	32.1	47.0	47.3	28.7	29.2	207.6	99.7	109.5	110.4	81.7	82.8

Table 8

Cumulative areas in the phase-space featuring a relative probability larger than 10^{-5} and 10^{-6} for the different types of phase-space plots – CM confocal measurement – SI stylus instrument – CM *vs.* ARS 30 µm, CM *vs.* ARS 900 µm – height distribution of CM combined with ARS angular measurement, SI *vs.* ARS 30 µm, SI *vs.* ARS 900 µm – height distribution of SI combined with ARS angular measurement.

CL No.	$A(p^*=10^{-5})$						$A(p^*=10^{-6})$					
	CM	*SI*	*CM vs. ARS 30 µm*	*CM vs. ARS 900 µm*	*SI vs. ARS 30 µm*	*SI vs. ARS 900 µm*	*CM*	*SI*	*CM vs. ARS 30 µm*	*CM vs. ARS 900 µm*	*SI vs. ARS 30 µm*	*SI vs. ARS 900 µm*
1	1666.8	380.7	448.0	450.7	245.4	247.0	3229.6	1035.1	719.2	719.6	446.4	446.4
2	2118.8	1363.0	542.3	497.8	451.9	412.0	3441.0	2022.8	741.1	708.7	615.3	615.3
3	2044.8	1017.2	486.9	488.3	341.2	340.2	2812.2	1526.8	585.8	584.0	459.8	459.8
4	2376.8	1012.7	725.6	725.1	488.5	488.5	4016.0	2091.3	919.6	917.2	776.9	776.9
5	443.1	192.9	154.7	158.8	115.0	120.2	722.1	348.8	207.4	209.3	167.4	167.4
6	842.2	284.6	278.5	279.0	180.7	180.8	2023.6	545.5	474.1	476.5	272.7	272.7
7	1152.4	320.7	309.8	311.9	194.7	194.8	2049.2	612.4	455.6	457.5	285.0	285.0
8	1226.7	799.6	357.6	358.0	372.4	371.9	2328.8	1589.7	550.2	551.3	545.0	545.0
9	2064.6	616.1	460.0	467.4	295.4	297.8	4127.3	1309.9	828.1	830.9	470.0	470.0
10	1270.4	513.4	326.4	330.6	235.7	237.8	1947.9	900.7	458.7	462.2	328.9	328.9
11	505.1	149.6	157.8	158.4	114.8	116.8	863.8	371.5	242.3	244.9	194.9	194.9
12	710.3	274.5	234.9	238.0	168.3	169.7	1392.4	602.9	383.3	387.4	274.5	274.5
13	780.2	486.9	255.5	258.3	241.9	243.8	1489.3	1235.5	385.2	387.0	493.9	493.9
14	887.7	379.8	273.3	276.1	191.0	194.4	1496.4	849.0	390.3	392.8	353.5	353.5
15	407.0	214.6	167.5	168.6	139.2	140.1	1052.4	479.9	302.0	304.1	230.3	230.3

Data availability

Data will be made available on request.

References

[1] K. Stout, Development of Methods for the Characterisation of Roughness in Three Dimensions, Penton Press, London, 2000.

[2] X. Jiang, P.J. Scott, D.J. Whitehouse, L. Blunt, Paradigm shifts in surface metrology. Part II. The current shift, Proc. R. Soc. A 463 (2007) 2071–2099.

[3] L. Blunt, X. Jiang, Advanced techniques for assessment surface topography: Development of a basis for 3D surface texture standards "SURFSTAND", Kogan Page Science, London, 2003.

[4] R. Leach (Ed.), Characterisation of Areal Surface Texture, Springer, Berlin, 2013.

[5] ISO 14406: Geometrical product specifications (GPS) - Extraction (ISO 14406: 2010), 2010.

[6] ISO 25178-601: Geometrical product specifications (GPS) - Surface texture: Areal - Part 601: Nominal characteristics of contact (stylus) instruments (ISO 25178-601: 2010), 2010.

[7] ISO 25178-603: Geometrical product specifications (GPS) - Surface texture: Areal - Part 603: Nominal characteristics of non-contact (phase-shifting interferometric microscopy) instruments (ISO 25178-603:2013), 2013.

[8] A. Walid, M. Eifler, Common Practices and Methodologies in scientific Functional characterization of surface topography, Metrology 5 (2) (2025) 33, https://doi.org/10.3390/metrology5020033.

[9] D.J. Whitehouse, The parameter rash – is there a cure? Wear 83 (1982) 75–78.

[10] H. Bodschwinna, W. Hillmann, Oberflächenmeßtechnik mit Tastschnittgeräten in der industriellen Praxis Beuth, Berlin Köln, 1992.

[11] ISO 13565-2 1996 GPS – Surface texture: Profile method; Surfaces having stratified functional properties – Part 2: Height characterization using the linear material ratio curve.

[12] ISO 21920-2: Geometrical product specifications (GPS) – Surface texture: Profile – Part 2: Terms, definitions and surface texture parameters (ISO 21920-2:2021, Corrected version 2022-06); German version EN ISO 21920-2:2022.

[13] ISO 13565-3 1998 GPS – Surface texture: Profile method; Surfaces having stratified functional properties Part 3: Height characterization using the material probability curve.

[14] ISO 25178-2: Geometrical product specifications (GPS) – Surface texture: Areal – Part 2: Terms, definitions and surface texture parameters (ISO 25178-2:2021).

[15] T.G. Mathia, P. Pawlus, M. Wieczorowski, Recent trends in surface metrology, Wear 271 (3–4) (2011) 494–508.

[16] L.D. Todhunter, R.K. Leach, S.D.A. Lawes, F. Blateyron, Industrial survey of ISO surface texture parameters, CIRP J. Manuf. Sci. Tech. 19 (2017) 84–92.

[17] P. Pawlus, T. Cieslak, T. Mathia, The study of cylinder liner plateau honing process, J. of Mat. Proc. Tech. 209 (20) (2009) 6078–6086.

[18] P. Pawlus, W. Grabon, The method of truncation parameters measurement from material ratio curve, Prec. Eng. 32 (4) (2008) 342–347.

[19] L.A. Franco, A. Sinatora, 3D surface parameters (ISO 25178-2): actual meaning of Spk and its relationship to Vmp, Prec. Eng 40 (2015) 106–111.

[20] L.J. Arantes, K.A. Fernandes, C.R. Schramm, J.E.S. Leal, A. Piratelli-Fillho, C. R. Franco, R.V. Arencibia, "The roughness characterization in cylinders obtained by conventional and flexible honing processes" Int, J. Adv. Manuf. Tech. 93 (2017) 635–649.

[21] A. Laukkanen, K. Holmberg, H. Ronkainen, G. Stachowiak, P. Podsiadlo, M. Wolski, M. Gee, C. Gachot, L. Li, Topographical orientation effects on surface stresses influencing on wear in sliding DLC contacts, Part 2: Modelling and simulations, Wear 388–389 (2017) 18–28.

[22] W. Rasp, C. Wichern, Effects of surface-topography directionality and lubrication condition on frictional behaviour during plastic deformation, J. Mater. Process. Technol. 125–126 (2002) 379–386.

[23] J. Seewig, M. Eifler, D. Hüser, R. Meeß, Rk material measure - a model-based design, Tech. Mess. 86 (9) (2019) 478–486.

[24] M. Eifler, K. Klauer, B. Kirsch, J.C. Aurich, J. Seewig, Performance verification of areal surface texture measuring instruments with the Sk-parameters, Measurement 173 (2021).

[25] C. Feng, X. Wang, Z. Yu, Neural networks modeling of honing surface roughness parameters defined by ISO 13565, J. Manuf. Syst. 21 (2023) 395–408.

[26] K. Deepak Lawrence, R. Shanmugamani, B. Ramamoorthy, Evaluation of image based Abbott–Firestone curve parameters using machine vision for the characterization of cylinder liner surface topography, Measurement 55 (2014) 318–334.

[27] W. Hartmann, Weckenmann A: Function-oriented Dimensional Metrology – More than Determining Size and Shape, in: Proc. of Sensor 2013, 16th International Conference on Sensors and Measurement Technology, 2013, pp. 285–290.

[28] J. Seewig, Praxisgerechte Signalverarbeitung zur Trennung der Gestaltabweichungen technischer Oberflächen, Shaker, Aachen, 2000.

[29] S. Rief, F. Ströer, S. Kieß, M. Eifler, J. Seewig, An approach for the simulation of ground and honed technical surfaces for training classifiers, Technologies 5 (4) (2017) 66, https://doi.org/10.3390/technologies5040066.

[30] J. Wu, Simulation of non-Gaussian surfaces with FFT, Tribol. Int. 37 (4) (2004) 339–346, https://doi.org/10.1016/j.triboint.2003.11.005.

[31] J.A. Ogilvy, J.R. Foster, Rough surfaces: gaussian or exponential statistics? J. Phys. D Appl. Phys. 22 (9) (1989) 1243–1251, https://doi.org/10.1088/0022-3727/22/9/001.

[32] G. Krolczyk, R. Maruda, P. Nieslony, M. Wieczorowski, Surface morphology analysis of Duplex Stainless Steel (DSS) in clean production using the power spectral density, Measurement 94 (2016) 464–470, https://doi.org/10.1016/j.measurement.2016.08.023.

[33] T.D.B. Jacobs, T. Junge, L. Pastewka, Quantitative characterization of surface topography using spectral analysis, Surf. Topogr. Metrol. Prop. 5 (1) (2017) 013001, https://doi.org/10.1088/2051-672x/aa51f8.

[34] M. Eifler, A. Keksel, J. Seewig, Comparison of material measures for the determination of transfer characteristics of surface topography measuring instruments, Surf. Topogr. Metrol. Prop. 7 (1) (2019) 015024, https://doi.org/10.1088/2051-672x/ab0dc6.

[35] A. Keksel, A.P. Lohfink, M. Eifler, C. Garth, J. Seewig, Virtual topography measurement with transfer functions derived by fitted time series models, Meas. Sci. Technol. 31 (5) (2019) 055008, https://doi.org/10.1088/1361-6501/ab5131.

[36] M. Eifler, J. Hering, J. Seewig, R.K. Leach, G. Von Freymann, X. Hu, G. Dai, Comparison of material measures for areal surface topography measuring instrument calibration, Surf. Topogr. Metrol. Prop. 8 (2) (2020) 025019, https://doi.org/10.1088/2051-672x/ab92ae.

[37] K. Klauer, M. Eifler, J. Seewig, B. Kirsch, J. Aurich, Application of function-oriented roughness parameters using confocal microscopy, Eng. Sci.Technol. Int. J. 21 (3) (2018) 302–313, https://doi.org/10.1016/j.jestch.2018.04.004.

[38] R.K. Leach, A. Hart, A comparison of stylus and optical methods for measuring 2D surface textures, NPL Report, CBTLM, 2002, p. 15.

[39] L. Koenders, R. Bergmans, J. Garnaes, J. Haycocks, N. Korolev, T. Kurosawa, F. Meli, B.C. Park, G.S. Peng, G.B. Picotto, E. Prieto, S. Gao, B. Smereczynska, T. Vorburger, G. Wilkening, Comparison on nanometrology: nano 2—step height, Metrologia 40 (1A) (2003) 04001, https://doi.org/10.1088/0026-1394/40/1a/04001.

[40] K. Doytchinov, F. Kornblit, C.C. Castellanos, J.C.V. Oliveira, T.B. Renegar, T. V. Vorburger, International comparison of surface roughness and step height (depth) standards, SIML-S2 (SIM 4.8), Metrologia 43 (1A) (2006) 04002.

[41] L. Koenders, P. Klapetek, F. Meli, G.B. Picotto, Comparison on step height measurements in the nano and micrometre range by scanning force microscopes, Metrologia 43 (1A) (2006) 04001, https://doi.org/10.1088/0026-1394/43/1a/04001.

[42] H.U. Danzebrink, L. Koenders, G.B. Picotto, A. Lassila, S.H. Wang, P. Klapetek, Final report on EUROMET.L-S15.a (EUROMET Project 925): Intercomparison on step height standards and 1D gratings, Metrologia 47 (1A) (2010) 04006, https://doi.org/10.1088/0026-1394/47/1a/04006.

[43] A. Baker, S.L. Tan, R. Leach, L. Jung, S.Y. Wong, A. Tonmueanwai, K. Naoi, J. Kim, T.B. Renegar, K.P. Chaudhary, O. Kruger, M. Amer, S. Gao, C.L. Tsai, N. Anh, A. Drijkarkara, Final report on APMP.L-K8: International comparison of surface roughness, Metrologia 50 (1A) (2013) 04003, https://doi.org/10.1088/0026-1394/50/1a/04003.

[44] R. Thalmann, A. Nicolet, F. Meli, G.B. Picotto, M. Matus, L. Carcedo, B. Hemming, O. Ganioglu, L. De Chiffre, F. Saraiva, S. Bergstrand, S. Zelenika, A. Tonmueanwai, C. Tsai, W. Shihua, O. Kruger, M.M. De Souza, J.A. Salgado, Z. Ramotowski, Calibration of surface roughness standards, Metrologia 53 (1A) (2015) 04001, https://doi.org/10.1088/0026-1394/53/1a/04001.

[45] G. Baršić, S. Mahović, G.B. Picotto, M.A. Amer, B. Runje, Groove depth measurements on roughness reference standards of the Croatian National Laboratory for Length (LFSB), Meas. Sci. Technol. 22 (9) (2011) 094020, https://doi.org/10.1088/0957-0233/22/9/094020.

[46] F.P. Bowden, D. Tarbor, The Friction and Lubrication of Solids, Clarendon Press, Oxford Classics Series, Oxford, 2001.

[47] J.A. Greenwood, J.B.P. Williamson, contact of nominally flat surfaces, Proc. Roy. Soc. Lond. Ser. A, Math. Phys. Sci. 295(1442) (1966) 300-319.

[48] J. Jocsak, V.W. Wong, E. Tomanik, T. Tian, The characterization and simulation of cylinder liner surface finishes. Proceedings of ICES2005 ASME Internal Combustion Engine Division 2005 Spring Technical Conference April 5-7, 2005, Chicago, IL, USA, 2005.

[49] E. Tomanik, Modelling of the Asperity Contact Area on Actual 3D Surfaces, SAE Technical Paper 2005-01-1864, 2005.

[50] D.J. Whitehouse, Handbook of Surface and Nanometrology, CRC Press, Boca Raton, FL, 2011.

[51] R.P. Nayak, Random Process Model of Rough Surfaces. Transactions of the ASME, July 1971, 1971, pp. 398–407.

[52] S. Hyun, L. Pei, J.F. Molinari, M.O. Robbins, Finite-element analysis of contact between elastic self-affine surfaces, Phys. Rev. E 70 (2004) 026117.

[53] V.L. Popov, What does Friction really Depend on? Robust Governing Parameters in Contact Mechanics and Friction, Phys. Mesomech. 19 (2) (2016) 115–122.

[54] N.O. Myers, Characterization of surface roughness, Wear 5 (1962) 182–189.

[55] B. Brodmann, H. Bodschwinna, Scattered light measurement on worm gears with high efficiency requirements, in: 3rd International Conference on Gear Production 2019, 2019.

[56] J. Seewig, G. Beichert, R. Brodmann, H. Bodschwinna, M. Wendel, Extraction of shape and roughness using scattering light, Proc. SPIE Int. Soc. Opt. Eng./Proc. SPIE 7389 (2009) 73890N, https://doi.org/10.1117/12.827478.

[57] M. Eifler, B. Brodmann, P.E. Hansen, J. Seewig, Traceable functional characterization of surface topography with angular-resolved scattering light measurement, Surf. Topogr. Metrol. Prop. 9 (3) (2021) 035042, https://doi.org/10.1088/2051-672x/ac2031.

[58] M. Eifler, B. Brodmann, B. Linke, A. Müller, J. Seewig, Comprehensive angular scattering distribution analysis for resource-efficient manufacturing, Proc. CIRP 120 (2023) 386–391, https://doi.org/10.1016/j.procir.2023.09.007.

[59] M. Eifler, B. Brodmann, A. Müller, J. Seewig, Comprehensive analysis of surfaces featuring functional characteristics by angular-resolved scattering light measurement, Proc. of SPIE Opt. Manuf. Test. 2024 (2024) 13134–13210, https://doi.org/10.1117/12.3026569.

[60] J. Seewig, P.J. Scott, M. Eifler, B. Barwick, D. Hüser, Crossing-the-line segmentation as a basis for Rsm and Rc evaluation, Surf. Topogr. Metrol. Prop. 8 (2020).

[61] VDA 2009, Geometrische Produktspezifikation - Oberflächenbeschaffenheit, winkelaufgelöste Streulichtmesstechnik, 2009. (guideline in German).

[62] B. Brodmann, M. Eifler, Surface Topography as an Energy State: Hamiltonian Description of Functional Properties in Phase Space and Quantification via Optical Methods, 2025. arXiv preprint https://doi.org/10.48550/arXiv.2503.01286.

[63] J. Seewig, B6.2 - the uncertainty of Roughness Parameters, Proc. Sens. 2011 (2013) 291–296, https://doi.org/10.5162/sensor2013/b6.2.

[64] ISO 25178-700, Geometrical product specifications (GPS) - Surface texture: Areal - Part 700: Calibration, adjustment and verification of areal topography measuring instruments (ISO 25178-700:2022), 2023.

[65] D.W. Scott, On optimal and data-based histograms, Biometrika 66 (3) (1979) 605–610, https://doi.org/10.1093/biomet/66.3.605.